Note: Supplementary information that is referenced in the text is provided at the bottom of the document.

Using fracture-scarp lineations as kinematic indicators on active normal fault scarps

Billy J. Andrews[1], Zoë K. Mildon[1], Manuel Diercks[1], Sam Mitchell[2], Gerald Roberts[2], Constanza Rodriguez Piceda[1], Jenni Robertson[2]

1. School of Geography, Earth and Environmental Sciences, Plymouth, United Kingdom
2. Birkbeck University of London, London, United Kingdom

Highlights

1 Fracture-scarp (F-S) lineations are mapped across eight bedrock fault scarps

2 F-S lineations may be split into en-echelon and parallel arrays

3 Kinematics and orientation of F-S lineations and arrays relate to the slip-vector

4 F-S lineations and arrays can act as kinematic markers on bedrock fault scarps

5 Kinematics of arrays provides insights into relative velocity across a fault plane

Key words

Slip-vector, active-tectonics, fault-scarp, earthquakes, fractures

Abstract

Reliable kinematic (slip vector) data collected from offset piercing points, corrugations or striations, is a key input for fault based seismic hazard assessments. However, it can be difficult to interpret kinematic indicators on degraded fault scarps. In this work, we investigate the orientations and growth history of on-fault fracture networks, which extend into the footwall and have greater preservation potential, to test whether they can be used to infer slip vector. We identify various F-S lineation patterns preserved across eight faults in Italy (Central Apennines) and Greece (Perachora Peninsula), including sinistral, dextral, and

parallel arrays. Our analysis reveals F-S lineations exhibit orientations that correlate with the measured slip vector, with kinematics of arrays related to slip-vector rake. Relative age relationships support a model of fracture growth where isolated en-echelon fractures evolve into interconnected networks during successive earthquakes, driven by footwall uplift and the intersection of a 3D strain ellipsoid with the fault plane. Further, we demonstrate F-S lineations and arrays may serve as reliable kinematic indicators, even on degraded fault scarps. Further analysis of on-fault fracture networks will enhance our understanding of earthquake dynamics, long-term fault behaviour, and may contribute to seismic hazard assessments through the identification of fault tips.

Supplementary

S1 – Summary of all faults and F-S maps used in this study

S2 – Data for mapped features

S3 – Summary of stereonet analysis and comparison between slip-vector and the rake of F-S lineations and arrays

S4– Step-by-step instructions for collection of F-S lineation data

S5 – Calculations of slip vector using F-S lineations and F-S arrays

S6 – Network Properties for relative ages

1. Introduction

Active continental normal faults host destructive surface rupturing earthquakes. For instance, the 1915 Avezzano earthquake (Ms 6.9) in the Central Apennines caused extensive damage and ~33,000 deaths in the Fucino Plain (Guidoboni et al., 2019). Consequently, undertaking robust seismic hazard assessments (SHA) within continental extensional regions is important, with many recent approaches adopting fault-based assessments (Pace et al., 2016; Faure Walker et al., 2021). Identifying potential seismogenic faults and measuring key parameters (e.g., fault dip, slip-vector, slip-rate, elapsed time since last earthquake, fault length) are crucial for fault-based seismic hazard assessments (Pace et al., 2016). Many of these parameters can be collected from bedrock fault scarps, and thus field-based observation play a pivotal role in fault-based SHA. These geomorphic features, common in many actively extending regions (e.g., Central Greece and the Italian Apennines), result from repeated surface rupturing earthquakes and are preserved since the last glacial maximum (Roberts and Michetti, 2004; Bubeck et al., 2015; Zou et al., 2021).

Bedrock fault scarps are comprised of fault rock and fractured footwall lithologies and 'free face' consisting of fault rocks in the footwall, with the hanging wall consisting of eroded footwall sediments such as alluvium, colluvium, or marine deposits (LEEDER et al., 1991; Tucker et al., 2011; Bubeck et al., 2015). Fault scarps offer prime exposures for collecting structural data along active normal faults (e.g., Roberts and Ganas, 2000; Roberts, 2007; Mildon et al., 2016). This has uncovered systematic slip-vector variations, with right-lateral slip on the left tip, and left-lateral slip on the right, converging towards the fault centre when the fault is viewed towards the footwall from the hangingwall (Roberts and Michetti, 2004; Papanikolaou and Roberts, 2007; Roberts, 2007; Faure Walker et al., 2010, 2021).

Convergent slip-vectors aid in determining if multiple surficial bedrock scarp outcrops belong to a single fault at depth (e.g., Ma and Kusznir, 1995; Roberts, 1996, 2007; Roberts and Ganas, 2000; Faure Walker et al., 2021), essential when assessing fault length for fault-based seismic hazard.

To determine slip vectors, one needs to measure kinematic indications along the length of the fault. Types of brittle kinematic indicators used on active faults include striations, steps, pull-apart structures, crescentic or trail markings, asymmetrically deformed clasts, corrugations, and piecing points (e.g., Hancock and Barka, 1987; Petit, 1987; Doblas et al., 1997). Between surface rupturing earthquakes, degradation of bedrock scarps occurs due to the erosion of the footwall (Allen and Densmore, 2000; Bilal et al., 2020). This leads to increased scarp roughness with height above the present-day scarp-colluvium contact (Tucker et al., 2011; Zou et al., 2021). This can lead to the erosion of subtle kinematic markers (e.g., striations) on degraded fault scarps, making the slip vector difficult to deduce.

Fractures are commonly observed but infrequently reported features that cut bedrock fault scarps that extend into the footwall, generally remaining well-preserved during scarp degradation except where vegetation or lichen covers the scarp. Examples include fractures forming around bends on 'wavy faults' (Chester and Chester, 2000); extension fractures perpendicular to fault slip (Friedman and Logan, 1970); comb fractures that have a distinct shape and are typically orientated perpendicular to the slip vector (Hancock and Barka, 1987; Stewart and Hancock, 1990; Smeraglia et al., 2018); slip vector parallel fractures (Hancock and Barka, 1987; Smeraglia et al., 2018); and pennant fractures that form en-echelon arrays along brittle shear planes and point in the direction of movement (Coelho et al., 2006; Lacazette, 2009). The identification of individual fractures, or fracture sets, has been used to infer slip vector on active faults in Western Türkiye (Hancock and Barka, 1987). However, fractures do not occur in isolation; rather, they form as arrays or networks (Aydin and Reches, 1982; Sanderson and Nixon, 2015; Peacock et al., 2016). Due to convergent slip vectors, the formation of bedrock scarps over multiple earthquake cycles, and non-characteristic earthquake ruptures (e.g., partial ruptures or multiple rupture patches), fracture patterns are expected to vary along a fault's length and encompass multiple generations of fractures resulting from successive earthquakes. It is therefore important to consider the length, orientation, kinematics, connectivity and growth history of the full network to gain insights into how the network evolved (Peacock and Sanderson, 2018) and thus to understand how they can be used to infer the slip vector.

Understanding how bedrock fracture networks form, evolve, and relate to the slip vector could help constrain slip vectors on faults lacking pristine surface outcrops and gain insights into how the footwall deforms across multiple seismic cycles. To investigate this, we document the type, kinematics and networks of fractures visible on fault planes, hereby termed fracture-scarp lineations from eight faults in Italy (Central Apennines) and Greece (Perachora Peninsula, Gulf of Corinth). By comparing observations of fracture orientation with slip vector measurements derived from striations and other kinematic indicators, we also present a methodology to systematically capture fracture data to infer the orientation of the slip vector.

2. Geological setting.

2.1 The Italian Apennines

The Central Apennines is a mountainous region of Italy that has been actively extending in a NE-SW orientation for the last 2 to 3 million years (Cavinato and Celles, 1999; Cavinato et al., 2002; Roberts et al., 2002; Roberts and Michetti, 2004; Montone and Mariucci, 2016). The mountain range initially formed as a fold and thrust belt with NE-SW shortening during the Miocene that thrusted Mesozoic and Cenozoic limestones onto Miocene Flysch deposits (Anderson and Jackson, 1987; Mazzoli et al., 2005; Vezzani et al., 2010). The switch from compression to extension has been attributed to various mechanisms, including rollback of the Adriatic plate (Patacca et al., 1993; Jolivet et al., 1998), the counter-clockwise rotation of the Adria microplate (e.g., Nocquet and Calais, 2004), or a slab window within the down going slab that enables upwelling mantle to drive extension (D'Agostino et al., 2001; Rosenbaum et al., 2008; Faure Walker et al., 2012). Regardless of the cause, this extension is responsible for the generation of a ~NW-SE trending normal fault system that cross cuts pre-existing thrust sheets (Barchi et al., 2021). Individual faults typically dip towards the WSW, have lengths of ~20 to 40 km and display total throws of less than 2 km (Pizzi and Scisciani, 2000; Roberts and Michetti, 2004; Faure Walker et al., 2021). Mapped fault strands are rarely physically connected (Faure Walker et al., 2021), but instead form an array of steeply dipping (~60˚) dip-slip faults that show en-echelon or end on fault tip arrangements with adjacent faults (Roberts and Michetti, 2004) (Fig 1a). Faults in the area have a long historical record of shallow (5 to 15 km), moderate-to-large (up to Mw 6.5 to 7.0) earthquakes stretching back to Roman times (Chiarabba et al., 2005; Rovida et al., 2016; Guidoboni et al., 2019). Extension rates across the central Apennines derived from focal mechanisms (1.6

mm/yr; Selvaggi, 1998), global positioning systems (2 to 3 mm/yr; D'Agostino et al., 2009) and Holocene fault scarps ($\leq 3.1^{+0.7}_{-0.4}$ mm/yr; Faure Walker et al., 2010) are low, and therefore the recurrence times of surface rupturing earthquakes on any given fault are high (100s to 1000s of years) (Cello et al., 1997; Galadini and Galli, 2000; Boncio et al., 2004; Galli et al., 2008; Galli, 2020).

2.2. The Gulf of Corinth

Greece has been actively extending in a north-south orientation for the past 5 million years (e.g., Ford et al., 2017), and similarly to the Central Apennines, extension overprints a pre-existing Cretaceous-Miocene Alpine fold-and-thrust belt (e.g., Billiris et al., 1991; Doutsos et al., 1993, 2006; Clarke et al., 1998; Roberts and Ganas, 2000). The driving forces behind the extension are believed to be a combination of slab roll back in the Hellenic subduction zone, and the dextral motion of the North Anatolian strike slip fault (Pichon and Angelier, 1979; Jackson, 1994; Jolivet et al., 1994, 2013, 2013; Le Pichon et al., 1995; Jolivet, 2001). This extension has resulted in an array of isolated ~E-W trending normal faults (Fig 1b). The faults have a long history of seismicity associated with them, with moderate-to-large earthquakes recorded as far back as 464 BC (Ambraseys and Jackson, 1990). The Gulf of Corinth is extending between ~5 and 11 mm/yr (Clarke et al., 1998; Briole et al., 2000, 2021; Chousianitis et al., 2015), with historical records suggesting that damaging earthquakes occur on the fault system every decade (Ambraseys and Jackson, 1990).

2.3 Typical bedrock scarp morphology of the studied faults

This study focuses on data collected from five faults within the Central Apennines (Mt Vettore, Martana-Terni, Fucino, Barete, and Campo Imperatore) and three faults situated on the Peracnora Peninsula at the eastern end of the Gulf of Corinth (Asprokambos, Pisia, and Skinos). The varying elapsed time since the most recent earthquake, spanning years to millennia, along with the differing elevations of exposed scarps, contributes to varying degrees of scarp degradation between sites. Studied faults exhibit similarities in their fault zone structure, characterised by bedrock fault scarps surrounded by minor fault arrays (e.g., Roberts, 2007). In a fault perpendicular direction, fault scarps consist of 10s of cm thick limestone fault rock (e.g., breccia and cataclasite), followed by intensely fractured host rock (e.g., Del Rio et al., 2023). In most cases, the hanging wall consists of colluvium and locally alluvium.

Surface ruptures occurred along the Pisia and Skinos faults during the 1981 eastern Gulf of Corinth seismic sequence (Jackson et al., 1982; Roberts, 1996a). These earthquakes caused extensive surface rupturing, often manifesting as isolated en-echelon segments with gaps between surface ruptures (Jackson et al., 1982; Mitchell et al., in prep). Ruptures on these faults are frequently situated within dense vegetation, and the preservation of scarps displays considerable variation both up the fault plane and along fault strike due to differing vegetation coverage and lithology cut by the fault. The 1981 seismic sequence increased interest in the eastern Gulf of Corinth, leading to the identification of several active faults in the region, including the Asprokambos fault (Leeder et al., 2005). In addition, the ruptured Pisia and Skinos faults have been investigated for geometry, kinematics, scarp morphology and palaeoseismology to improve our understanding of slip characteristics and fault growth (Jackson et al., 1982; Roberts, 1996b; Collier et al., 1998; Roberts and Ganas, 2000; Mechernich et al., 2018).

3 Methods

Field measurements were taken using a compass clinometer and the FieldMOVE Clino application on an ISO mobile device. The device's accuracy was verified in the field by comparing measurements to those taken with a compass clinometer before data collection. Bedrock scarp orientations and kinematic markers (striations, corrugations, tool marks, and gouge ribbons) were measured at each field site where present. In cases of limited observed lineations, additional data from the same fault collected on previous field campaigns were included. In most cases, it was not possible to measure the planes of fractures cutting the scarp, so instead we measured and analysed the intersection lineations of fractures with the fault scarp (Fracture-Scarp (F-S) lineations). Three classifications of F-S lineations were observed and corresponding measurements were taken:

- *Parallel F-S lineations (Fig 2a):* Isolated or series of parallel lineations, often matching the slip-vector trend in our examples. Measurements: Rake and length of the F-S lineation.
- *En-echelon arrays (Fig 2b):* Commonly observed, showing sinistral or dextral shear indicators, and with variable F-S lineation trace and array lengths. Measurements: kinematics of array, rake and length of F-S lineations, and rake and length of the array.
- *Parallel arrays (Fig 2c):* Similar to en-echelon arrays but less common, displaying no shear indicators, and with shorter F-S lineation trace lengths compared to en-echelon arrays and parallel F-S lineations. Measurements: Rake and length of F-S lineations, and rake and length of the array.

The above F-S lineations and arrays combined to create a lineation network where the presence and relative proportion of each classification differed between localities. Rake may be measured in either a clockwise or anticlockwise manner and in this study we opted for the first approach whereby a rake of 90° represents pure normal faulting. It should be noted that certain authors (e.g., Aki and Richards, 1980) employed the anticlockwise approach, which results in negative values during comparison.

To complement field data, high-resolution images capturing key features were taken orthogonal to the fault plane for subsequent digitisation. In QGIS, manual lineament mapping of F-S lineations were undertaken at a constant scale for each photograph, with direct comparisons avoided between data collected at different scales on the same fault. This is because fracture patterns are often scale-dependant (Bertrand et al., 2015; Forstner and Laubach, 2022), so comparing across scales could lead to erroneous conclusions. Additionally, all mapping was undertaken by the lead author to limit discrepancies between datasets caused by the subjective biases of different interpreters (Andrews et al., 2019). Post-digitisation, F-S lineations were visually classified based on the scheme introduced above (Fig 2). Subsequently, the orientations and array trends were quantified and converted to rake. These data were then portrayed as histograms and stereographic projections, with the mean fault plane of the imaged area serving as the fault plane. Employing average fault plane measurements could induce minor errors in F-S lineation and array orientations where the fault plane is non-planar; however, the effect is expected to be minimal and unlikely to impact the overall conclusions drawn from the data.

For all localities, we compare the orientation of F-S lineation and arrays with the slip-vector measured from imagery and in the field. We do this by calculating the mean vector and

Bingham analysis of each dataset in Stereonet 10 (Allmendinger et al., 2013; Cardozo and Allmendinger, 2013), as well as by assigning clusters through a visual analysis of contoured datasets and assessing rake histograms. For derived clusters we report the trend and plunge of the mode, and the angular spread of the data across the fault plane. Additionally, we compare the rake of F-S lineations and arrays to the slip-vector by taking the mean vector of mapped lineations, or when not present, the equivalent rake of any field derived value.

To investigate the evolution of F-S lineation network length and connectivity during the earliest stages of fracture development (up to 15 cm), we analyse three sub-sections from the bedrock fault scarp at Mt Vettore. In each area, we interpret age relationships within the fracture network using topological and cross-cutting relationships. Each sub-section represents a progressively advanced stage of fracture evolution, indicated by the increasing number of age relationships from panels (i) to (iii). For each sub-section, we assess trace-length distributions, fracture intensity, and network connectivity for each interpreted stage of fracture evolution. Fracture intensity was calculated by dividing the total fracture length of fractures at a given age relationship by the area of the subsection (e.g., Dershowitz and Einstein, 1988). To assess connectivity, we analysed network topology, defining the network as a series of nodes (isolated (I), abutting (Y), and crossing (X)) and branches (isolated (I-I), partly isolated (I-C), and fully connected (C-C)) (Manzocchi, 2002; Sanderson and Nixon, 2015, 2018). Based on node type proportions, we calculated the percentage of connected nodes (Pc) using the following equation:

$$P_c = \frac{(3N_Y + 4N_X)}{(N_I + 3N_Y + 4N_X)} \quad \text{(Equation 1)}$$

where N_I is the number of isolated nodes, N_I is the number of abutting nodes, and N_I is the number of crossing nodes. We then compare results from each interpreted stage of the fracture evolution to gain insights into F-S lineation development.

4 Results

4.1: F-S lineation networks

The spatial distribution and orientation of F-S lineations and arrays are examined using lineament maps, which include the original photographs showing key features alongside the interpreted F-S lineation network (black lines), including the classified F-S arrays (red, purple, and blue dashed lines). The orientation of mapped lineations, F-S lineation, and F-S arrays are shown using stereographic projections, constructed from the rake of mapped fractures.

4.1.1: F-S lineations

Abundant on-fault fractures (F-S lineations) were observed across all studied fault scarps (Figs 3, 4), with fracture length ranging from 0.005 m to 20.85 m. Only the largest fractures extend into the scarp beyond the decimeter-thick limestone fault rock. Some larger fractures show small offsets indicating shear, however, most fractures were tight with no observable aperture, complicating the classification of deformation mode. F-S lineations occur as arrays, with dextral, sinistral, and parallel kinematics. Most fractures are unfilled, except for localised vuggy calcite at Terni-Martana and mineralised fractures at the Mt Vettore.

The Mt. Vettore locality, with a fault scarp height ranging from ~3 to ~20 meters, provides particularly good exposure of F-S lineations (Fig 3). The outcrop spans a prominent fault bend with a ~30° variation in fault strike from ESE to SSE (Fig. 3c), resulting in mean fault plane orientations with strikes from 116° to 149° and dips from 54° to 82°. Despite changes in fault plane orientation, mapped striation trends remain consistent, ranging from 262° to 283° (Fig. 3c, d). This locality exhibits varied footwall degradation, from pristine sections within the coseismically exposed “white ribbon” to degraded zones where fractures remain well preserved, allowing F-S lineations to be mapped at scales of 1:50, 1:10 and 1:1. We describe these data prior to discussing trends observed at other localities.

Across Mt Vettore, fracture orientation, connectivity, and length vary by location and the map scale (Fig 3). At the largest scale (1:50), F-S lineations form a well-connected network with a maximum trace length of 20.9 m and mean of 1.6 m. At the 1:10 scale, the network is less connected, with a mean trace length of 0.5 m. At the 1:1,F-S lineations shorter than 5 cm are visible that exhibit ow sinuosity, while longer fractures show multiple changes in rake (e.g., Fig 3f). Smaller trace length arrays intersect larger F-S lineations, often connecting longer (>5 m) F-S lineations. The spread of rake values increases at the smallest scale (1:1), showing more connections between F-S lineations with different trace lengths.

Across other sites, most F-S lineations are isolated, with high network connectivity localised to small areas or where footwall degradation is high (Fig 4, S1-6). While F-S trends show peaks, variability in rakes between and within maps is observed, with some maps showing a bi-modal distribution of F-S rake corresponding to oppositely dipping F-S lineations (e.g., Barete, Fig S4a). Small trace-length off-trend F-S lineations are locally observed connecting longer F-S lineaitons (Fig 4a), or at the intersection of F-S lineaitons (Fig S2, S3b). At Campo Imperatore, F-S lineations exhibit high connectivity and a large spread in F-S lineation trend (Fig S2).

Trace length distributions across faults show shallow gradients with abrupt jumps, suggesting characteristic F-S lineation lengths for a given map (Fig 5). Across all datasets, the upper portion of the data displays an increase in gradient away from the characteristic length (Fig 5a). This is particularly clear when data is limited to between 0.01 and 0.15 m, with the gradient change occurring for most faults between 60 and 70% of the data and each map displaying a different characteristic length (Fig 5b). When these lengths are cross-referenced to the fracture maps, it appears that the switch from characteristic F-S lineation length to non-characteristic occurs for features that show a sinuous trace and cut through smaller F-S lineations (e.g., Fig 3f). Initial fracture growth is further discussed in section 4.2.

4.1.2: F-S lineation arrays

F-S lineations could be visually grouped into arrays for all maps, with sinistral and dextral, and, in fewer cases (15 out of 19 maps), parallel arrays observed (Figs 3-5). At Mt. Vettore, mapping scale influenced the proportion of array types and orientations of arrays. For less connected F-S lineation networks (1:10 and 1:1 scales), arrays up to ~0.4 m in length primarily consisted of isolated F-S lineations (Fig 3). Sinistral arrays made up >50% of arrays across all scales, with dextral arrays exceeding parallel arrays (Figs 3-5). Sinistral and parallel arrays showed similar orientations across scales, with array rakes within 40-70° of the slip vector. Conversely, dextral arrays showed greater rake variability, with a bi-modal distribution at the 1:50 scale and a broader range across all scales, often occurring at a high angle to the slip vector (Fig 4, S5).

Array orientations varied across other faults and maps (Figs 4, S1-6). While orientations differed between maps, the dominant array type for each map displayed a prominent orientation cluster (Fig 4). Like Mt. Vettore, the less common array type exhibited a wider spread in orinetaiton, often with broad or multiple peaks. For instance, the Skinos fault shows tightly clustered sinistral and parallel arrays around 54°/040°, while dextral arrays displayed greater spread with multiple peaks (Fig 4c). This variation often arises from commonly observed, shallowly dipping, short trace length arrays aligned ~90° to the main trend.

Array lengths displayed a negatively skewed distribution, with medians consistently below means (Fig 5c). The shortest arrays (bottom 5-30%) display gradual length increases, with a characteristic length for medium length arrays (40-80%), and a substantial increase in gradient for the largest arrays. Longer arrays, consisting of longer F-S lineations, often bound blocks of fault scarp that contain smaller trace length arrays (Fig 3e, 4a). Array length distributions also varied by shear sense (Fig 5d). For instance, sinistral arrays were longest on the Pisia fault, whereas dextral arrays were longest at two of the three Barete localities. Generally, the most abundant arrays were also the longest, though there were exceptions, and parallel arrays were typically shorter than dextral or sinistral arrays (Fig 5d). Overall, array shear sense, orientation, and length appear to be influenced by slip vector rake, F-S lineation connectivity, dominant array type, and fault plane geometry.

4.2 Relative age relationships between F-S lineations

Three areas were selected within the ‘white ribbon’ at Mt Vettore to display a range of key features and were selected to demonstrate how the network differs between where the dominant fractures are more isolated (Fig 6a), show evidence of fracture growth and linkage (Fig 6b), and are dominated by well-connected fractures (Fig 6c). En-echelon arrays are common across all areas, with most fractures displaying abutting or cross-cutting relationships (Fig 6). Isolated large trace-length (> 10 cm) fractures display tip-damage zones, wing cracks, and rake deviations where fractures intersect smaller en-echelon arrays (Fig 6a). In more connected networks (Fig 6b, c), sinuous fracture traces, trailing segments, and abrumpt rake changes (~90°in Fig. 6c) indicate interactions between large and pre-existing fractures. Evidence of abandoned tips, linking damage zones, and transfer zones suggest progressive strain localisation onto larger fractures. In Figures 6b and 6c, the largest fractures show shear offsets (<0.5 cm) and bound smaller trace-length fractures and arrays like observations made at other localities (Figs 3, 4, S1-6).

During the initial fracture evolution (relative age 1), all sub-sections display low-to-medium fracture intensity (18.9 to 48.5 fm^{-1}) consisting of en-echelon, and locally parallel, arrays of F-S lineations. The network is largely isolated (Pc = 0.00 to 0.02), with 3 to 8% censored fractures and a characteristic length of 2.5 to 3 cm for ~70% of fractures (Fig 7). As fractures evolve (relative age 2), some fractures lengthen and abut against those from relative age 1, increasing the fracture intensity (33.3 to 77.8 fm^{-1}), proportion of censored fractures (15 to 15%), and the connectivity of the network (Pc = 0.15 to 0.43). The length distribution also shifts, particularly among the longest 15 to 20% of fractures.

With further fracture development (relative ages 3 to 6), fracture intensity and connectivity continue to increase (Fig 6, 7). Length distributions and the proportion of censored fractures show only slight deviations, as new fractures often localise at the intersections of larger fractures, while small, early fractures remain isolated. In panels 6b and 6c, the network complexity is higher, with fracture growth becoming increasingly localised on larger fractures that bound blocks of smaller fractures as strain localises onto these structures (Figs 6, 7).

In addition to fractures, additional fault rock products are preserved at Mt Vettore such as fault breccias, veins and tool marks that were not observed on any other fault scarps in this study (Fig 3, 6). Fault breccias are elongate, sub-parallel to the slip vector, and contain angular to sub-angular clasts (3mm to 4 cm) that can often be matched to adjacent sections of fault scarp (Fig 6a). The breccia matrix consists of microcrystalline calcite or reworked fine-grained fault rock that occasionally exhibits S-C fabrics indicative of sinistral shear (Fig 6a). Locally, hairline calcite veins (<3 cm in length) form parallel or en-echelon arrays (Fig 3f, S1). Calcite veins cross-cut breccias and are, in turn, cross-cut by F-S lineations. Though beyond the scope of this study, these observations imply progressive deformation of the footwall prior to fracture development.

4.3 F-S lineation networks across variable fault geometries

Non-planar fault surfaces, such as those with corrugations, influence the distribution and orientation of F-S lineations and arrays (Figs 3, 4, S2-6). Figure 8 highlights a corrugation, where F-S lineation rake changes notably across both the ridge and trough. The Asprokambos locality, which is characterised by abundant variations in dip and dip-direction across the outcrop, further demonstrates how non-planar fault geometries affect F-S lineation networks (Fig 9). Here, the orientation of striations varies widely, with both divergence and convergent slip vectors observed (Fig 9a). Geometrical complexity influences the orientation of F-S lineations (Fig 9c) and the kinematics of F-S arrays (Fig 9d). This is most clearly observed in the parallel arrays (red lines), which diverge and converge around corrugations. Individual corrugations commonly have sinistral and dextral arrays on either ridge, with parallel arrays in trough (Fig 9d). Fracture intensity is greatest along corrugation ridges, and there is an increase in shallowly dipping arrays where dip changes are observed (Fig 9d, e). These observations indicate that non-planar fault geometries, particularly those with corrugations, significantly influence the orientation and distribution of F-S lineations and arrays. Variations in slip-vector rake across ridges and troughs lead to divergence and convergence of F-S lineations, while fracture intensity is highest along corrugation ridges. This suggests that where slip is not orthogonal to the fault plane, the kinematics and intensity of F-S arrays are notably altered, highlighting the importance of fault plane geometry in on-fault fracture formation.

4.4 Orientation of F-S lineaitions and arrays relative to the slip vector

Median slip-vector rake ranged from 70° to 135° and for most faults, the spread of lineation rake was small with interquartile ranges of <10°. This enabled us to explore how the trend of F-S lineations and arrays relative to the measured slip vector varied between fracture maps. When comparing the relative orientation of F-S lineations and arrays to the slip vector, patterns emerge that link the rake of the slip vector to the types and orientation of features (Fig 10). F-S lineation histograms for all data exhibit peaks at +45° and -45°, with large standard deviations. When the data is analysed by fault map, faults with slip-vector rakes under 90° show a peak at +45°, while those with rakes over 90° showed a peak at -45°. The proportion of sinistral to dextral arrays also appears to be influenced by the rake of the slip vector with dextral arrays dominating where the slip vector rake is <<90°; sinistral arrays dominating when the slip vector rake is >>90°, and all types, including conjugate fracture sets, present when the slip vector rake is ~90°. When the data is normalised to remove the effect of shear sense, the trend for F-S lineations (Fig 10b) and arrays (Fig 10c) become clearer, with primary peaks for F-S lineations at 40°-45° (with a broad spread up to 55°), 0°-5°, and 80°-90° relative to the slip vector. Arrays display a prominent peak within 5° of the slip vectors (with a broad spread up to 10°), and a minor peak at 80° to 85°. Additionally, where both dextral and sinistral arrays are present, the conjugate bisector of F-S lineation peaks aligns with the slip vector. Despite these general rules, there is scatter in the data, which appears to correlate to corrugations on the fault plane, small arrays that form at the intersection or between large trace length F-S lineations, or variable fault geometry. These findings highlight the complex relationship between slip-vector rake and the orientation of F-S lineations and arrays, with deviations largely influenced by fault corrugations, intersecting arrays, and variations in fault geometry.

Discussion

5.1 Model of on-fault fracture growth on bedrock fault scarps

In order to confidently use on-fault fractures to infer slip-vector information, it is first important to present a model of how the fracture network forms. On-fault fractures are common (e.g., Hancock and Barka, 1987); however, how individual fractures evolve into fracture networks is rarely examined. Our data indicates that the geometry of on-fault fractures relate to the slip-vector inferred from striations and that during the initial stages, fracture networks initially form as isolated, small fractures in en-echelon arrays with a consistent spacing between F-S lineations (Figs 3, 4, 6). As deformation of the fault scarp continues, the strain accommodated by the fracture network becomes localised onto a sub-set of on-fault fractures that continue to increase in length and occasionally display minor offsets, whilst other on-fault fractures no longer accrue strain and become isolated (Fig 6). We propose that because we observe on-fault fractures to be predominantly constrained to the fault core, they are not associated with prior deformation (e.g. thrusting), but instead form in response to co-seismic or post-seismic slip during, or following, normal faulting earthquakes.

Traditional models of on-fault fractures formed by fault slip assume they form as mode 1 fractures that are perpendicular to the slip vector, developing when the intermediate principal stress ($\sigma 2$) is parallel to the fault plane (Wilson et al., 2003; Blenkinsop, 2008; Scholz, 2019). However, our observations of en-echelon F-S lineations suggest fractures do not always form perpendicular to the averaged slip-vector. One explanation for this is that fractures form in response to different rupture directions, caused by differences in rupture patches between earthquakes (e.g., Kato, 2020). While this cannot be discounted, you may expect to see similar dispersion in the slip-vector derived from striations and/or corrugations, as well as cross-cutting striations (e.g., Andrews et al., 2020). This is not observed at Mt Vettore, where the dispersion in both field and photo derived striations is very low when compared to the wide array of observed fracture orientations (Fig 3). Another explanation for fractures that do not form perpendicular to the slip vector is that they developed under a stress state whereby the intermediate stress axis ($\sigma2$) is oblique to fault strike (e.g., Cruikshank et al., 1991; Crider and Peacock, 2004; Blenkinsop, 2008). This could occur where the strike and/or dip of the fault plane varies with respect to the orientation of the stress axis. This occurs across a range of scales within fault bends, corrugations, and oblique fault segments (e.g., Withjack et al., 1995; Ferrill et al., 1999; Walsh et al., 1999; Peacock, 2002; Iezzi et al., 2018; Mitchell et al., 2024), where the inferred average slip vector remains consistent around fault bends (Iezzi et al., 2018), suggesting that the orientation of the principal stress axis remain consistent. Therefore, the orientation and shape of the resultant 3D strain ellipsoid would also be expected to remain constant, with the trend of principle strain axis aligned to the regional slip vector. Depending on the relative orientation of the fault plane to the local slip-vector averaged over multiple earthquakes (e.g., derived from corrugations), the rake of the slip vector on the fault plane may exceed or fall below 90° (Fig 11b), which combined with any change in fault dip causing the intersection of the fault plane and 3D ellipsoid to resemble a 2D strain ellipse with a sinistral or dextral shear sense (Fig 11d, e).

It is well known that the orientation of the stress axis relative to the fault rotates near the surface, due to the free surface effect, as well as in close vicinity to the fault plane (e.g., Reiter, 2021). Therefore, the shape of the strain ellipsoid at a particular point on the fault is unlikely to remain constant through time. Instead, as throw accumulates, footwall uplift will change in the shape of the strain ellipsoid as the effective normal stress decreases (Fig 11c). At depth (100s m), the strain ellipsoid is prolate causing localised brecciation of the mineralised fault core and the formation of striations, but no on-fault fractures. As the footwall continues to uplift the intermediate strain ellipsoid axis increases and isolated en-echelon fractures begin to form. During initial fracture growth, fracture length and spacing varied between faults, but were similar for individual fracture maps and fractures did not penetrate beyond the mineralised fault core (Fig 5, 6).

As the on-fault fracture network continues to develop, fracture intensity and connectivity increase, and strain within the fracture network becomes localised onto a subset of on-fault fractures, which increase in length (Fig 11). As linking fractures grow, it is probable they extend beyond the fault core and into the footwall lithologies. This is observed at Mt Vettore, where erosion along large trace length fractures extends beyond the fault scarp (Fig 3b, e). As strain becomes localised onto this subset, the spacing between actively deforming fractures increases, with evidence of slip along the F-S lineation occasionally evidenced (Fig 6c). Slip along on-fault fractures, and the interaction between fractures as the network becomes more connected, leads to the development of damage zone features (cf., Caine et al., 1996; Wibberley et al., 2008; Faulkner et al., 2010) that consist of well-connected small trace length fractures. Damage zone fractures increase network connectivity, but due to only being small, have only a small effect on the intensity and trace length distribution of the network (Fig 7). Like observations on normal faults (e.g., (Peacock et al., 2017; Nixon et al., 2020; Hansberry et al., 2021), damage zone fractures preferentially form where there are geometrical complexities along the through-going fracture. For example, at bends that formed when isolated arrays linked during the initial stages of fracture growth (Fig 6).

Further strain accommodated within the on-fault fracture network during successive earthquakes will be accommodated by larger trace length connected fractures, leaving blocks of small trace-length, layer-bound, fractures that retain the fracture pattern of the initial stages of fracture growth (Figs 6, 11). As fault-rock products, striations, isolated F-S arrays, and through-going fractures show consistent geometries relative to the inferred slip vector, it is likely that for a given site, the relative orientation of the fault plane to the slip vector remained constant across multiple seismic cycles both prior to, and during fracture development. This model explains the progressive fracture growth as well as why similar fracture patterns, characteristic lengths, and orientations are observed across a range of scales and different faults.

5.2 Inferring slip vectors using on-fault fractures

Previous studies have suggested that individual measurements of comb or pinnate fractures can be utilised to derive slip vectors (Hancock and Barka, 1987; Smeraglia et al., 2018). However, our findings demonstrate fractures form at a range of angles that deviate from typical slip-perpendicular or slip-parallel orientations. It is therefore important to consider the orientation of all fractures and arrays that constitute the fracture network. Where this is done, the generic rules presented in Fig 10 can be used infer the slip-vector from the rake distributions of F-S lineations and arrays (see Supplementary 4 for detailed workflow).

The test the effectiveness of the method, we apply the generic rules derived from the entire dataset to each fault individually, infer the slip vector, and then compare the inferred slip vector to the measured slip vector (Table 1, Fig 12). In 12 out of 19 cases, the rake of the slip vector could be inferred to within 5°, and all but the map of the corrugation on the Skinos fault (Fig 8) were within 10° of the measured value. This precision was only possible when the inferred slip vector from F-S lineations and F-S arrays relationships were calculated separately (Fig 12a), and then the mean of both taken (Fig 12b). In every instance, the error in the inferred rake remained within the range of slip vectors measured from the imagery (Fig 12b). Based on these rakes, the average absolute difference in slip vector trend and plunge is 6.2° and 2.2° respectively, which fall within the expected measurement error for field observations (Fig 12c, d).

We have demonstrated that on-fault fracture networks can be used to derive the slip vector on active normal faults. However, it is important to note that, due to biases in fracture data collection, a fracture network extracted from imagery or field observations is non-unique and may vary between interpreters. Therefore, it is crucial to account for these potential variations by considering the following guidelines when applying the method. First, the nature of footwall deformation should be assessed in the field to ensure that photo-lineaments extracted from digital data represent actual structures. This approach has been shown to reduce uncertainty during manual lineament analysis (Andrews et al., 2019; Peacock et al., 2019) and has been undertaken for all faults in the Central Apennines with findings from these faults used to guide fracture mapping on faults in the Gulf of Corinth. Additionally, the field classification of fractures enables key information to be gathered (e.g., fracture type, fill, kinematics) that provide important information about fracture formation (Peacock and Sanderson, 2018). Secondly, the quality of imagery used for interpretation must be sufficiently high to allow confident identification of field structures, and the interpretation should be performed at a constant and appropriate scale of observation (Scheiber et al., 2015; Andrews et al., 2019). Maintaining consistency in the imaged area and ensuring the scale is such the image is not pixelated ensures that the imaged network is consistent between study sites. Finally, fracture mapping is subject to subjective biases influenced by factors such as the interpreter's experience and style, the scientific question being addressed, fatigue during interpretation, and group dynamics (Burns and Brown, 1978; Gillespie et al., 2011; Scheiber et al., 2015; Andrews et al., 2019; Peacock et al., 2019). Andrews et al. (2019) demonstrated that interpreters tend to be internally consistent in their interpretation style and reiterated the importance of establishing a pre-set criteria prior to fracture mapping (Andrews et al., 2019; Gillespie et al., 2011). We recommend that interpretation is conducted by a single experienced interpreter to ensure consistency across different sample areas. If this is not feasible, we suggest a subset of the data is interpreted collectively by all interpreters to ensure standardised mapping techniques (Andrews et al., 2019). Additionally, reanalysing a subset of the data (e.g., 10%) can help quantify the magnitude of uncertainty introduced to the dataset by subjective bias (Gillespie et al., 2011). By addressing these considerations, we believe this method offers a valuable additional constraint on the slip vector of active normal faults.

The ability to use on-fault fractures to infer slip vectors is particularly useful for fault scarps with different levels of footwall degradation (Table 1, Fig 12). Indeed, we have shown that slip vectors can be reliably inferred even where abundant kinematic markers are absent. For example, at Campo Imperatore, no striations were visible, however, the data still aligned with the measured corrugation trend (Table 1). The method is less reliable in cases where the F-S network has high trace lengths and is well connected (Fig 3f), where the fault plane is highly irregular and only the mean slip vector can be deduced (Fig 8, 9), or where arrays develop along the T-axis (Fig S5a). Despite this, F-S lineation patterns serve as dependable kinematic indicators, even on degraded bedrock scarps. This is especially valuable in areas of low extension rates and with long recurrence intervals, where fault scarps can undergo significant degradation between earthquakes (e.g., Italy).

Conclusions

In this study, we focus on the orientations of F-S lineations and arrays and their relationship to the observed slip vector. Our analysis reveals that F-S lineations and arrays consistently exhibit orientations that correlate with the inferred slip vector, with kinematics related to the rake of the slip-vector. We propose a model of on-fault fracture growth in which isolated en-echelon fractures evolve into interconnected networks during successive earthquakes, driven by the intersection of an evolving 3D strain ellipsoid with the fault plane. Initially, footwall deformation is constrained to breccia formation, however, as footwall uplift causes a drop in the effective normal stress acting on the fault, fracture formation within the mineralised fault core occurs. The kinematics recorded in the breccia and fractures are similar, suggesting the slip-vector remains consistent across multiple seismic cycles at the studied sites. Progressive fracture growth leads to the formation of through-going fractures, that localise strain and develop damage zones whilst bounding blocks of isolated small trace length F-S lineations and arrays. These networks reflect the kinematic history of the fault and provide insights into the dynamics of earthquake slip across multiple earthquake cycles. Due to the predictable orientation of on-fault fractures relative to the slip-vector, we demonstrate F-S lineations and arrays may act as a reliable further constraint when inferring slip-vector. We suggest further analysis of on-fault fracture networks could benefit earthquake science by providing information about long-term fault behaviour and fault linkage.

References

Aki, K., Richards, P.G., 1980. Richards, Paul G., and Keiiti Aki. Quantitative seismology: theory and methods. Freeman, San Francisco, CA.

Allen, P.A., Densmore, A.L., 2000. Sediment flux from an uplifting fault block. Basin Research 12, 367–380. https://doi.org/10.1111/j.1365-2117.2000.00135.x

Allmendinger, R.W., Cardonzo, N.C., Fisher, D., 2013. Structural Geology Algorithms: Vectors & Tensors. Cambridge University Press, Cambridge, UK.

Ambraseys, N.N., Jackson, J.A., 1990. Seismicity and associated strain of central Greece between 1890 and 1988. Geophysical Journal International 101, 663–708. https://doi.org/10.1111/j.1365-246X.1990.tb05577.x

Anderson, H., Jackson, J., 1987. The deep seismicity of the Tyrrhenian Sea. Geophysical Journal International 91, 613–637. https://doi.org/10.1111/j.1365-246X.1987.tb01661.x

Andrews, B.J., Roberts, J.J., Shipton, Z.K., Bigi, S., Tartarello, M.C., Johnson, G., 2019. How do we see fractures? Quantifying subjective bias in fracture data collection. Solid Earth 10, 487–516. https://doi.org/10.5194/se-10-487-2019

Andrews, B.J., Shipton, Z.K., Lord, R., McKay, L., 2020. The growth of faults and fracture networks in a mechanically evolving, mechanically stratified rock mass: a case study from Spireslack Surface Coal Mine, Scotland. Solid Earth 11, 2119–2140. https://doi.org/10.5194/se-11-2119-2020

Aydin, A., Reches, Z., 1982. Number and orientation of fault sets in the field and in experiments. Geology 10, 107–112. https://doi.org/10.1130/0091-7613(1982)10<107:NAOOFS>2.0.CO;2

Barchi, M.R., Carboni, F., Michele, M., Ercoli, M., Giorgetti, C., Porreca, M., Azzaro, S., Chiaraluce, L., 2021. The influence of subsurface geology on the distribution of earthquakes during the 2016-–2017 Central Italy seismic sequence. Tectonophysics 807, 228797. https://doi.org/10.1016/j.tecto.2021.228797

Bertrand, L., Géraud, Y., Le Garzic, E., Place, J., Diraison, M., Walter, B., Haffen, S., 2015. A multiscale analysis of a fracture pattern in granite: A case study of the Tamariu granite, Catalunya, Spain. Journal of Structural Geology 78, 52–66. https://doi.org/10.1016/j.jsg.2015.05.013

Bilal, A., McClay, K., Scarselli, N., 2020. Fault-scarp degradation in the central Exmouth Plateau, North West Shelf, Australia. Geological Society, London, Special Publications 476, 231–257. https://doi.org/10.1144/SP476.11

Billiris, H., Paradissis, D., Veis, G., England, P., Featherstone, W., Parsons, B., Cross, P., Rands, P., Rayson, M., Sellers, P., Ashkenazi, V., Davison, M., Jackson, J., Ambraseys, N., 1991. Geodetic determination of tectonic deformation in central Greece from 1900 to 1988. Nature 350, 124–129. https://doi.org/10.1038/350124a0

Blenkinsop, T.G., 2008. Relationships between faults, extension fractures and veins, and stress. Journal of Structural Geology 30, 622–632. https://doi.org/10.1016/j.jsg.2008.01.008

Boncio, P., Lavecchia, G., Pace, B., 2004. Defining a model of 3D seismogenic sources for Seismic Hazard Assessment applications: The case of central Apennines (Italy). Journal of Seismology 8, 407–425. https://doi.org/10.1023/B:JOSE.0000038449.78801.05

Briole, P., Ganas, A., Elias, P., Dimitrov, D., 2021. The GPS velocity field of the Aegean. New observations, contribution of the earthquakes, crustal blocks model. Geophysical Journal International 226, 468–492. https://doi.org/10.1093/gji/ggab089

Briole, P., Rigo, A., Lyon-Caen, H., Ruegg, J.C., Papazissi, K., Mitsakaki, C., Balodimou, A., Veis, G., Hatzfeld, D., Deschamps, A., 2000. Active deformation of the Corinth rift, Greece: Results from repeated Global Positioning System surveys between 1990 and 1995. Journal of Geophysical Research: Solid Earth 105, 25605–25625. https://doi.org/10.1029/2000JB900148

Bubeck, A., Wilkinson, M., Roberts, G.P., Cowie, P.A., McCaffrey, K.J.W., Phillips, R., Sammonds, P., 2015. The tectonic geomorphology of bedrock scarps on active normal faults in the Italian Apennines mapped using combined ground penetrating radar and terrestrial laser scanning. Geomorphology, Geomorphology of Active Faulting and Seismic Hazard Assessment: New Tools and Future Challenges 237, 38–51. https://doi.org/10.1016/j.geomorph.2014.03.011

Burns, K.L., Brown, G.H., 1978. The human perception of geological lineaments and other discrete features in remote sensing imagery: Signal strengths, noise levels and quality. Remote Sensing of Environment 7, 163–176. https://doi.org/10.1016/0034-4257(78)90045-7

Caine, J.S., Evans, J.P., Forster, C.B., 1996. Fault zone architecture and permeability structure. Geology 24, 1025–1028. https://doi.org/10.1130/0091-7613(1996)024<1025:FZAAPS>2.3.CO;2

Cardozo, N., Allmendinger, R.W., 2013. Spherical projections with OSXStereonet. Computers & Geosciences 51, 193–205. https://doi.org/10.1016/j.cageo.2012.07.021

Cavinato, G.P., Carusi, C., Dall'Asta, M., Miccadei, E., Piacentini, T., 2002. Sedimentary and tectonic evolution of Plio–Pleistocene alluvial and lacustrine deposits of Fucino Basin (central Italy). Sedimentary Geology, Lacustrine Depositional Systems 148, 29–59. https://doi.org/10.1016/S0037-0738(01)00209-3

Cavinato, G.P., Celles, P.G.D., 1999. Extensional basins in the tectonically bimodal central Apennines fold-thrust belt, Italy: Response to corner flow above a subducting slab in retrograde motion. Geology 27, 955–958. https://doi.org/10.1130/0091-7613(1999)027<0955:EBITTB>2.3.CO;2

Cello, G., Mazzoli, S., Tondi, E., Turco, E., 1997. Active tectonics in the central Apennines and possible implications for seismic hazard analysis in peninsular Italy. Tectonophysics 272, 43–68. https://doi.org/10.1016/S0040-1951(96)00275-2

Chester, F.M., Chester, J.S., 2000. Stress and deformation along wavy frictional faults. Journal of Geophysical Research: Solid Earth 105, 23421–23430. https://doi.org/10.1029/2000JB900241

Chiarabba, C., Jovane, L., DiStefano, R., 2005. A new view of Italian seismicity using 20 years of instrumental recordings. Tectonophysics 395, 251–268. https://doi.org/10.1016/j.tecto.2004.09.013

Chousianitis, K., Ganas, A., Evangelidis, C.P., 2015. Strain and rotation rate patterns of mainland Greece from continuous GPS data and comparison between seismic and geodetic moment release. Journal of Geophysical Research: Solid Earth 120, 3909–3931. https://doi.org/10.1002/2014JB011762

Clarke, P.J., Davies, R.R., England, P.C., Parsons, B., Billiris, H., Paradissis, D., Veis, G., Cross, P.A., Denys, P.H., Ashkenazi, V., Bingley, R., Kahle, H.-G., Muller, M.-V., Briole, P., 1998. Crustal strain in central Greece from repeated GPS measurements in the interval 1989–1997. Geophysical Journal International 135, 195–214. https://doi.org/10.1046/j.1365-246X.1998.00633.x

Coelho, S., Passchier, C., Marques, F., 2006. Riedel-shear control on the development of pennant veins: Field example and analogue modelling. Journal of Structural Geology 28, 1658–1669. https://doi.org/10.1016/j.jsg.2006.05.009

Collier, R.E.L., Pantosti, D., D'Addezio, G., De Martini, P.M., Masana, E., Sakellariou, D., 1998. Paleoseismicity of the 1981 Corinth earthquake fault: Seismic contribution to extensional strain in central Greece and implications for seismic hazard. Journal of

Geophysical Research: Solid Earth 103, 30001–30019. https://doi.org/10.1029/98JB02643

Crider, J.G., Peacock, D.C.P., 2004. Initiation of brittle faults in the upper crust: a review of field observations. Journal of Structural Geology 26, 691–707. https://doi.org/10.1016/j.jsg.2003.07.007

Cruikshank, K.M., Zhao, G., Johnson, A.M., 1991. Analysis of minor fractures associated with joints and faulted joints. Journal of Structural Geology 13, 865–886. https://doi.org/10.1016/0191-8141(91)90083-U

D'Agostino, N., Jackson, J.A., Dramis, F., Funiciello, R., 2001. Interactions between mantle upwelling, drainage evolution and active normal faulting: an example from the central Apennines (Italy). Geophysical Journal International 147, 475–497. https://doi.org/10.1046/j.1365-246X.2001.00539.x

D'Agostino, N., Mantenuto, S., D'Anastasio, E., Avallone, A., Barchi, M., Collettini, C., Radicioni, F., Stoppini, A., Fastellini, G., 2009. Contemporary crustal extension in the Umbria–Marche Apennines from regional CGPS networks and comparison between geodetic and seismic deformation. Tectonophysics, Ten Years after the Umbria-Marche Earthquake, Central Italy 476, 3–12. https://doi.org/10.1016/j.tecto.2008.09.033

Del Rio, L., Moro, M., Masoch, S., Doumaz, F., Saroli, M., Cavallo, A., Di Toro, G., 2023. Architecture of active extensional faults in carbonates: Campo Felice and Monte D'Ocre faults, Italian Apennines. Journal of Structural Geology 169, 104828. https://doi.org/10.1016/j.jsg.2023.104828

Dershowitz, W.S., Einstein, H.H., 1988. Characterizing rock joint geometry with joint system models. Rock Mechanics and Rock Engineering 21, 21–51. https://doi.org/10.1007/BF01019674

Doblas, M., Mahecha, V., Hoyos, M., Lo´pez-ruiz, J., 1997. Slickenside and fault surface kinematic indicators on active normal faults of the Alpine Betic Cordilleras, Granada, southern Spain. Journal of Structural Geology 19, 159–170. https://doi.org/10.1016/S0191-8141(96)00086-7

Doutsos, T., Koukouvelas, I.K., Xypolias, P., 2006. A new orogenic model for the External Hellenides. Geological Society, London, Special Publications 260, 507–520. https://doi.org/10.1144/GSL.SP.2006.260.01.21

Doutsos, T., Pe-Piper, G., Boronkay, K., Koukouvelas, I., 1993. Kinematics of the central Hellenides. Tectonics 12, 936–953. https://doi.org/10.1029/93TC00108

Faulkner, D.R., Jackson, C.A.L., Lunn, R.J., Schlische, R.W., Shipton, Z.K., Wibberley, C.A.J., Withjack, M.O., 2010. A review of recent developments concerning the structure, mechanics and fluid flow properties of fault zones. Journal of Structural Geology, Fault Zones 32, 1557–1575. https://doi.org/10.1016/j.jsg.2010.06.009

Faure Walker, J., Boncio, P., Pace, B., Roberts, G., Benedetti, L., Scotti, O., Visini, F., Peruzza, L., 2021. Fault2SHA Central Apennines database and structuring active fault data for seismic hazard assessment. Scientific Data 8, 87. https://doi.org/10.1038/s41597-021-00868-0

Faure Walker, J.P., Roberts, G.P., Cowie, P.A., Papanikolaou, I., Michetti, A.M., Sammonds, P., Wilkinson, M., McCaffrey, K.J.W., Phillips, R.J., 2012. Relationship between topography, rates of extension and mantle dynamics in the actively-extending Italian Apennines. Earth and Planetary Science Letters 325–326, 76–84. https://doi.org/10.1016/j.epsl.2012.01.028

Faure Walker, J.P., Roberts, G.P., Sammonds, P., Cowie, P.A., 2010. Comparison of earthquake strains over 102 and 104 year timescales: Insights into variability in the seismic cycle in the central Apennines, Italy. Journal of Geophysical Research: Solid Earth 115. https://doi.org/10.1029/2009JB006462

Ferrill, D.A., Stamatakos, J.A., Sims, D., 1999. Normal fault corrugation: implications for growth and seismicity of active normal faults. Journal of Structural Geology 21, 1027–1038. https://doi.org/10.1016/S0191-8141(99)00017-6

Ford, M., Hemelsdaël, R., Mancini, M., Palyvos, N., 2017. Rift migration and lateral propagation: evolution of normal faults and sediment-routing systems of the western Corinth rift (Greece). Geological Society, London, Special Publications 439, 131–168. https://doi.org/10.1144/SP439.15

Forstner, S.R., Laubach, S.E., 2022. Scale-dependent fracture networks. Journal of Structural Geology 165, 104748. https://doi.org/10.1016/j.jsg.2022.104748

Friedman, M., Logan, J.M., 1970. Influence of residual elastic strain on the orientation of experimental fractures in three quartzose sandstones. Journal of Geophysical Research (1896-1977) 75, 387–405. https://doi.org/10.1029/JB075i002p00387

Galadini, F., Galli, P., 2000. Active Tectonics in the Central Apennines (Italy) – Input Data for Seismic Hazard Assessment. Natural Hazards 22, 225–268. https://doi.org/10.1023/A:1008149531980

Galli, P., 2020. Recurrence times of central-southern Apennine faults (Italy): Hints from palaeoseismology. Terra Nova 32, 399–407. https://doi.org/10.1111/ter.12470

Galli, P., Galadini, F., Pantosti, D., 2008. Twenty years of paleoseismology in Italy. Earth-Science Reviews 88, 89–117. https://doi.org/10.1016/j.earscirev.2008.01.001

Gillespie, M.R., Barnes, R.P., Milodowski, A.E., 2011. British Geological Survey scheme for classifying discontinuities and fillings. British Geological Survey Research Report RR/10/05, 56.

Guidoboni, E., Ferrari, G., Tarabusi, G., Sgattoni, G., Comastri, A., Mariotti, D., Ciuccarelli, C., Bianchi, M.G., Valensise, G., 2019. CFTI5Med, the new release of the catalogue of strong earthquakes in Italy and in the Mediterranean area. Scientific Data 6, 80. https://doi.org/10.1038/s41597-019-0091-9

Hancock, P.L., Barka, A.A., 1987. Kinematic indicators on active normal faults in Western Turkey. Journal of Structural Geology 9, 573–584. https://doi.org/10.1016/0191-8141(87)90142-8

Hansberry, R.L., King, R.C., Holford, S.P., Hand, M., Debenham, N., 2021. How wide is a fault damage zone? Using network topology to examine how fault-damage zones overprint regional fracture networks. Journal of Structural Geology 146, 104327. https://doi.org/10.1016/j.jsg.2021.104327

Iezzi, F., Mildon, Z., Walker, J.F., Roberts, G., Goodall, H., Wilkinson, M., Robertson, J., 2018. Coseismic Throw Variation Across Along-Strike Bends on Active Normal Faults: Implications for Displacement Versus Length Scaling of Earthquake Ruptures. Journal of Geophysical Research: Solid Earth 123, 9817–9841. https://doi.org/10.1029/2018JB016732

Jackson, J., 1994. Active Tectonics of the Aegean Region. Annual Review of Earth and Planetary Sciences 22, 239–271. https://doi.org/10.1146/annurev.ea.22.050194.001323

Jackson, J.A., Gagnepain, J., Houseman, G., King, G.C.P., Papadimitriou, P., Soufleris, C., Virieux, J., 1982. Seismicity, normal faulting, and the geomorphological development of the Gulf of Corinth (Greece): the Corinth earthquakes of February and March 1981. Earth and Planetary Science Letters 57, 377–397. https://doi.org/10.1016/0012-821X(82)90158-3

Jolivet, L., 2001. A comparison of geodetic and finite strain pattern in the Aegean, geodynamic implications. Earth and Planetary Science Letters 187, 95–104. https://doi.org/10.1016/S0012-821X(01)00277-1

Jolivet, L., Daniel, J.M., Truffert, C., Goffé, B., 1994. Exhumation of deep crustal metamorphic rocks and crustal extension in arc and back-arc regions. Lithos, Tectonics, Metamorphism and Magmatism in Island Arcs 33, 3–30. https://doi.org/10.1016/0024-4937(94)90051-5

Jolivet, L., Faccenna, C., Goffé, B., Mattei, M., Rossetti, F., Brunet, C., Storti, F., Funiciello, R., Cadet, J.P., d'Agostino, N., Parra, T., 1998. Midcrustal shear zones in postorogenic extension: Example from the northern Tyrrhenian Sea. Journal of Geophysical Research: Solid Earth 103, 12123–12160. https://doi.org/10.1029/97JB03616

Jolivet, L., Faccenna, C., Huet, B., Labrousse, L., Le Pourhiet, L., Lacombe, O., Lecomte, E., Burov, E., Denèle, Y., Brun, J.-P., Philippon, M., Paul, A., Salaün, G., Karabulut, H., Piromallo, C., Monié, P., Gueydan, F., Okay, A.I., Oberhänsli, R., Pourteau, A., Augier, R., Gadenne, L., Driussi, O., 2013. Aegean tectonics: Strain localisation, slab tearing and trench retreat. Tectonophysics, The Aegean: A Natural Laboratory for Tectonics - Neotectonics 597–598, 1–33. https://doi.org/10.1016/j.tecto.2012.06.011

Kato, N., 2020. Complexity in the Earthquake Cycle Increases with the Number of Interacting Patches. Pure and Applied Geophysics 177, 4657–4676. https://doi.org/10.1007/s00024-020-02555-4

Lacazette, A., 2009. Paleostress analysis from image logs using pinnate joints as slip indicators. AAPG Bulletin 93, 1489–1501. https://doi.org/10.1306/08110909087

Le Pichon, X., Chamot-Rooke, N., Lallemant, S., Noomen, R., Veis, G., 1995. Geodetic determination of the kinematics of central Greece with respect to Europe: Implications for eastern Mediterranean tectonics. Journal of Geophysical Research: Solid Earth 100, 12675–12690. https://doi.org/10.1029/95JB00317

Leeder, M.R., Portman, C., Andrews, J.E., Collier, R.E.Ll., Finch, E., Gawthorpe, R.L., McNeill, L.C., Pérez-Arlucea, M., Rowe, P., 2005. Normal faulting and crustal deformation, Alkyonides Gulf and Perachora peninsula, eastern Gulf of Corinth rift, Greece. Journal of the Geological Society 162, 549–561. https://doi.org/10.1144/0016-764904-075

LEEDER, M.R., SEGER, M.J., STARK, C.P., 1991. Sedimentation and tectonic geomorphology adjacent to major active and inactive normal faults, southern Greece. Journal of the Geological Society 148, 331–343. https://doi.org/10.1144/gsjgs.148.2.0331

Ma, X.Q., Kusznir, N.J., 1995. Coseismic and postseismic subsurface displacements and strains for a dip-slip normal fault in a three-layer elastic-gravitational medium. Journal of Geophysical Research: Solid Earth 100, 12813–12828. https://doi.org/10.1029/95JB00674

Manzocchi, T., 2002. The connectivity of two-dimensional networks of spatially correlated fractures. Water Resources Research 38, 1-1-1–20. https://doi.org/10.1029/2000WR000180

Mazzoli, S., Pierantoni, P.P., Borraccini, F., Paltrinieri, W., Deiana, G., 2005. Geometry, segmentation pattern and displacement variations along a major Apennine thrust zone, central Italy. Journal of Structural Geology 27, 1940–1953. https://doi.org/10.1016/j.jsg.2005.06.002

Mechernich, S., Schneiderwind, S., Mason, J., Papanikolaou, I.D., Deligiannakis, G., Pallikarakis, A., Binnie, S.A., Dunai, T.J., Reicherter, K., 2018. The Seismic History of the Pisia Fault (Eastern Corinth Rift, Greece) From Fault Plane Weathering Features and Cosmogenic 36Cl Dating. Journal of Geophysical Research: Solid Earth 123, 4266–4284. https://doi.org/10.1029/2017JB014600

Mildon, Z.K., 2017. The link between earthquakes and structural geology; the role of elapsed time, 3D geometry and stress transfer in the central Apennines, Italy.

Mildon, Z.K., Roberts, G.P., Faure Walker, J.P., Wedmore, L.N.J., McCaffrey, K.J.W., 2016. Active normal faulting during the 1997 seismic sequence in Colfiorito, Umbria: Did slip propagate to the surface? Journal of Structural Geology 91, 102–113. https://doi.org/10.1016/j.jsg.2016.08.011

Mitchell, S., Roberts, G.P., Faure Walker, J.P., Iezzi, F., Sgambato, C., Robertson, J., Mildon, Z.K., Ganas, A., Papanikolaou, I.D., Rugen, E.J., 2024. The relationship between kinematics and fault geometry for surface coseismic ruptures on across-strike faults: New observations of slip vectors and displacements along the Pisia and Skinos faults from the 1981 Eastern Gulf of Corinth, Greece earthquakes. Journal of Structural Geology 182, 105117. https://doi.org/10.1016/j.jsg.2024.105117

Montone, P., Mariucci, M.T., 2016. The new release of the Italian contemporary stress map. Geophysical Journal International 205, 1525–1531. https://doi.org/10.1093/gji/ggw100

Moretti, I., Sakellariou, D., Lykousis, V., Micarelli, L., 2003. The Gulf of Corinth: an active half graben? Journal of Geodynamics, Active Faults: Analysis, Processes and Monitoring 36, 323–340. https://doi.org/10.1016/S0264-3707(03)00053-X

Nixon, C.W., Nærland, K., Rotevatn, A., Dimmen, V., Sanderson, D.J., Kristensen, T.B., 2020. Connectivity and network development of carbonate-hosted fault damage zones from western Malta. Journal of Structural Geology 141, 104212. https://doi.org/10.1016/j.jsg.2020.104212

Nocquet, J.-M., Calais, E., 2004. Geodetic Measurements of Crustal Deformation in the Western Mediterranean and Europe. Pure and Applied Geophysics 161, 661–681. https://doi.org/10.1007/s00024-003-2468-z

Pace, B., Visini, F., Peruzza, L., 2016. FiSH : MATLAB Tools to Turn Fault Data into Seismic-Hazard Models. Seismological Research Letters 87, 374–386. https://doi.org/10.1785/0220150189

Papanikolaou, I.D., Roberts, G.P., 2007. Geometry, kinematics and deformation rates along the active normal fault system in the southern Apennines: Implications for fault growth. Journal of Structural Geology 29, 166–188. https://doi.org/10.1016/j.jsg.2006.07.009

Patacca, E., Sartori, R., Scandone, P., 1993. Tyrrhenian Basin and Apennines. Kinematic Evolution and Related Dynamic Constraints. In: Boschi, E., Mantovani, E., Morelli, A. (Eds.), Recent Evolution and Seismicity of the Mediterranean Region, NATO ASI Series. Springer Netherlands, Dordrecht, 161–171. https://doi.org/10.1007/978-94-011-2016-6_7

Peacock, D.C.P., 2002. Propagation, interaction and linkage in normal fault systems. Earth-Science Reviews 58, 121–142. https://doi.org/10.1016/S0012-8252(01)00085-X

Peacock, D.C.P., Dimmen, V., Rotevatn, A., Sanderson, D.J., 2017. A broader classification of damage zones. Journal of Structural Geology 102, 179–192. https://doi.org/10.1016/j.jsg.2017.08.004

Peacock, D.C.P., Nixon, C.W., Rotevatn, A., Sanderson, D.J., Zuluaga, L.F., 2016. Glossary of fault and other fracture networks. Journal of Structural Geology 92, 12–29. https://doi.org/10.1016/j.jsg.2016.09.008

Peacock, D.C.P., Sanderson, D.J., 2018. Structural analyses and fracture network characterisation: Seven pillars of wisdom. Earth-Science Reviews 184, 13–28. https://doi.org/10.1016/j.earscirev.2018.06.006

Peacock, D.C. p, Sanderson, D.J., Bastesen, E., Rotevatn, A., Storstein, T.H., 2019. Causes of bias and uncertainty in fracture network analysis. Norwegian Journal of Geology 99, 113–128. https://doi.org/10.17850/njg99-1-06

Petit, J.P., 1987. Criteria for the sense of movement on fault surfaces in brittle rocks. Journal of Structural Geology 9, 597–608. https://doi.org/10.1016/0191-8141(87)90145-3

Pichon, X.L., Angelier, J., 1979. The hellenic arc and trench system: A key to the neotectonic evolution of the eastern mediterranean area. Tectonophysics 60, 1–42. https://doi.org/10.1016/0040-1951(79)90131-8

Pizzi, A., Scisciani, V., 2000. Methods for determining the Pleistocene–Holocene component of displacement on active faults reactivating pre-Quaternary structures: examples from the Central Apennines (Italy). Journal of Geodynamics 29, 445–457. https://doi.org/10.1016/S0264-3707(99)00053-8

Reiter, K., 2021. Stress rotation – impact and interaction of rock stiffness and faults. Solid Earth 12, 1287–1307. https://doi.org/10.5194/se-12-1287-2021

Roberts, G.P., 2007. Fault orientation variations along the strike of active normal fault systems in Italy and Greece: Implications for predicting the orientations of subseismic-resolution faults in hydrocarbon reservoirs. AAPG Bulletin 91, 1–20. https://doi.org/10.1306/08300605146

Roberts, G.P., 1996a. Noncharacteristic normal faulting surface ruptures from the Gulf of Corinth, Greece. Journal of Geophysical Research: Solid Earth 101, 25255–25267. https://doi.org/10.1029/96JB02119

Roberts, G.P., 1996b. Variation in fault-slip directions along active and segmented normal fault systems. Journal of Structural Geology 18, 835–845. https://doi.org/10.1016/S0191-8141(96)80016-2

Roberts, G.P., Ganas, A., 2000. Fault-slip directions in central and southern Greece measured from striated and corrugated fault planes: Comparison with focal mechanism and geodetic data. Journal of Geophysical Research: Solid Earth 105, 23443–23462. https://doi.org/10.1029/1999JB900440

Roberts, G.P., Michetti, A.M., 2004. Spatial and temporal variations in growth rates along active normal fault systems: an example from The Lazio–Abruzzo Apennines, central Italy. Journal of Structural Geology 26, 339–376. https://doi.org/10.1016/S0191-8141(03)00103-2

Roberts, G.P., Michetti, A.M., Cowie, P., Morewood, N.C., Papanikolaou, I., 2002. Fault slip-rate variations during crustal-scale strain localisation, central Italy. Geophysical Research Letters 29, 9-1-9–4. https://doi.org/10.1029/2001GL013529

Rosenbaum, G., Gasparon, M., Lucente, F.P., Peccerillo, A., Miller, M.S., 2008. Kinematics of slab tear faults during subduction segmentation and implications for Italian magmatism. Tectonics 27. https://doi.org/10.1029/2007TC002143

Rovida, A., Locati, M., Camassi, R., Lolli, B., Gasperini, P., Antonucci, A., 2016. Catalogo Parametrico dei Terremoti Italiani CPTI15, versione 4.0.

Sanderson, D.J., Nixon, C.W., 2018. Topology, connectivity and percolation in fracture networks. Journal of Structural Geology 115, 167–177. https://doi.org/10.1016/j.jsg.2018.07.011

Sanderson, D.J., Nixon, C.W., 2015. The use of topology in fracture network characterization. Journal of Structural Geology 72, 55–66. https://doi.org/10.1016/j.jsg.2015.01.005

Scheiber, T., Fredin, O., Viola, G., Jarna, A., Gasser, D., Łapińska-Viola, R., 2015. Manual extraction of bedrock lineaments from high-resolution LiDAR data: methodological bias and human perception. GFF 137, 362–372. https://doi.org/10.1080/11035897.2015.1085434

Scholz, C.H., 2019. The Mechanics of Earthquakes and Faulting. Cambridge University Press.

Selvaggi, G., 1998. Spatial distribution of horizontal seismic strain in the Apennines from historical earthquakes. Annali Di Geofisica 41.

Smeraglia, L., Bernasconi, S.M., Berra, F., Billi, A., Boschi, C., Caracausi, A., Carminati, E., Castorina, F., Doglioni, C., Italiano, F., Rizzo, A.L., Uysal, I.T., Zhao, J., 2018. Crustal-scale fluid circulation and co-seismic shallow comb-veining along the longest normal fault of the central Apennines, Italy. Earth and Planetary Science Letters 498, 152–168. https://doi.org/10.1016/j.epsl.2018.06.013

Stewart, I.S., Hancock, P.L., 1990. Brecciation and fracturing within neotectonic normal fault zones in the Aegean region. Geological Society, London, Special Publications 54, 105–110. https://doi.org/10.1144/GSL.SP.1990.054.01.11

Tucker, G.E., McCoy, S.W., Whittaker, A.C., Roberts, G.P., Lancaster, S.T., Phillips, R., 2011. Geomorphic significance of postglacial bedrock scarps on normal-fault footwalls. Journal of Geophysical Research: Earth Surface 116. https://doi.org/10.1029/2010JF001861

Vezzani, L., Festa, A., Ghisetti, F.C., 2010. Geology and Tectonic Evolution of the Central-southern Apennines, Italy. Geological Society of America.

Walsh, J.J., Watterson, J., Bailey, W.R., Childs, C., 1999. Fault relays, bends and branch-lines. Journal of Structural Geology 21, 1019–1026. https://doi.org/10.1016/S0191-8141(99)00026-7

Wibberley, C.A.J., Yielding, G., Toro, G.D., 2008. Recent advances in the understanding of fault zone internal structure: a review. Geological Society, London, Special Publications 299, 5–33. https://doi.org/10.1144/SP299.2

Wilson, J.E., Chester, J.S., Chester, F.M., 2003. Microfracture analysis of fault growth and wear processes, Punchbowl Fault, San Andreas system, California. Journal of Structural Geology 25, 1855–1873. https://doi.org/10.1016/S0191-8141(03)00036-1

Withjack, M.O., Islam, Q.T., La Pointe, P.R., 1995. Normal Faults and Their Hanging-Wall Deformation: An Experimental Study. AAPG Bulletin 79, 1–17. https://doi.org/10.1306/8D2B1494-171E-11D7-8645000102C1865D

Zou, J., He, H., Yokoyama, Y., Sproson, A.D., Shirahama, Y., Zhou, Y., Wei, Z., Shi, F., Geng, S., 2021. Identification of Paleoearthquakes and Coseismic Slips on a Normal Fault Using High-Precision Quantitative Morphology: Application to the Jiaocheng Fault in the Shanxi Rift, China. Lithosphere 2021, 2550879. https://doi.org/10.2113/2021/2550879

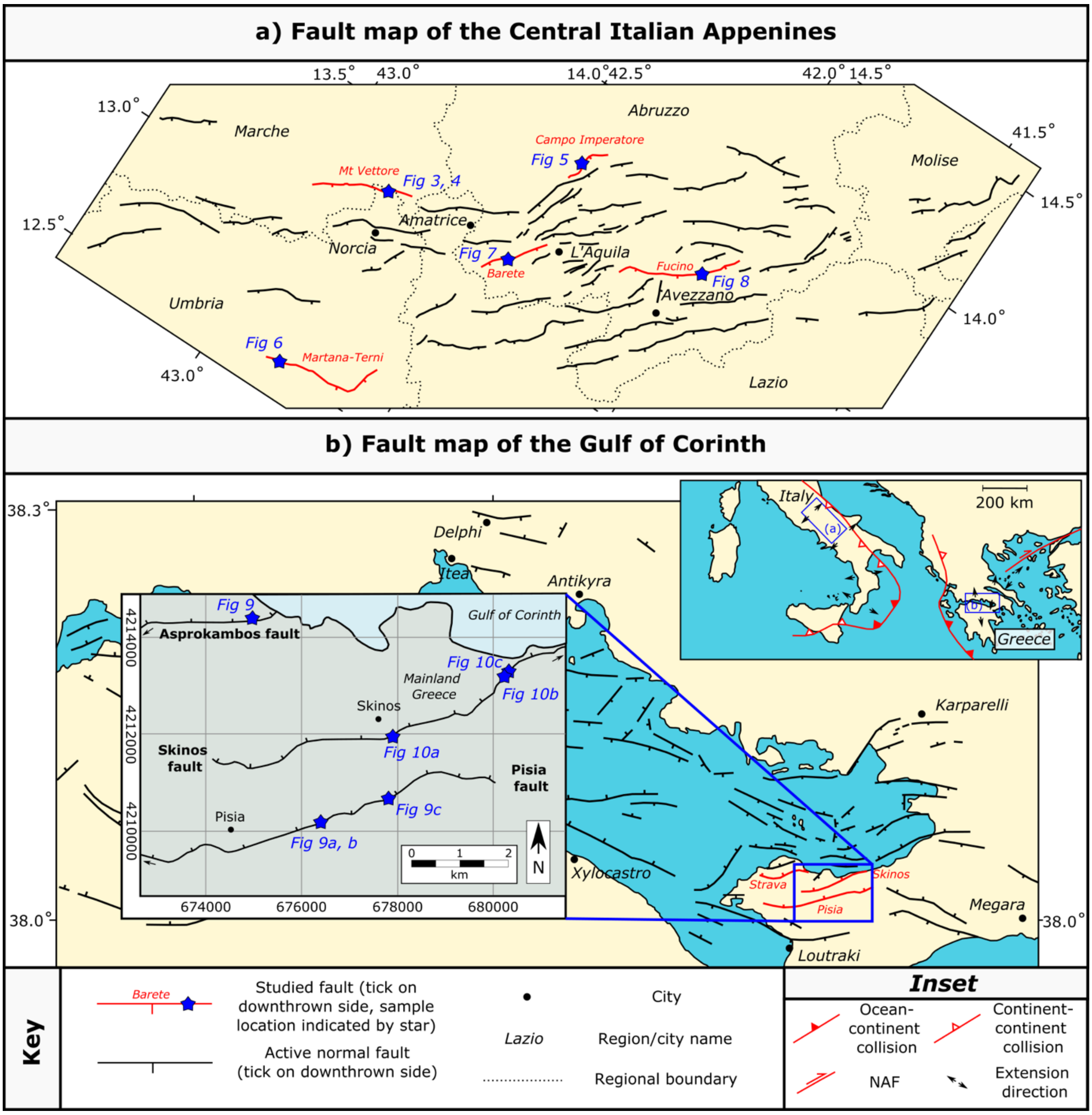

Figure 1: Fault map showing the location of studied faults: a) Fault map of the active faults in Central Italy (Mildon, 2017); b) fault map of the Gulf of Corinth, showing the location of studied faults on the Perachora Peninsula (after Moretti et al., 2003). The inset summarises the regional tectonics of the eastern Mediterranean (after Roberts, 2007).

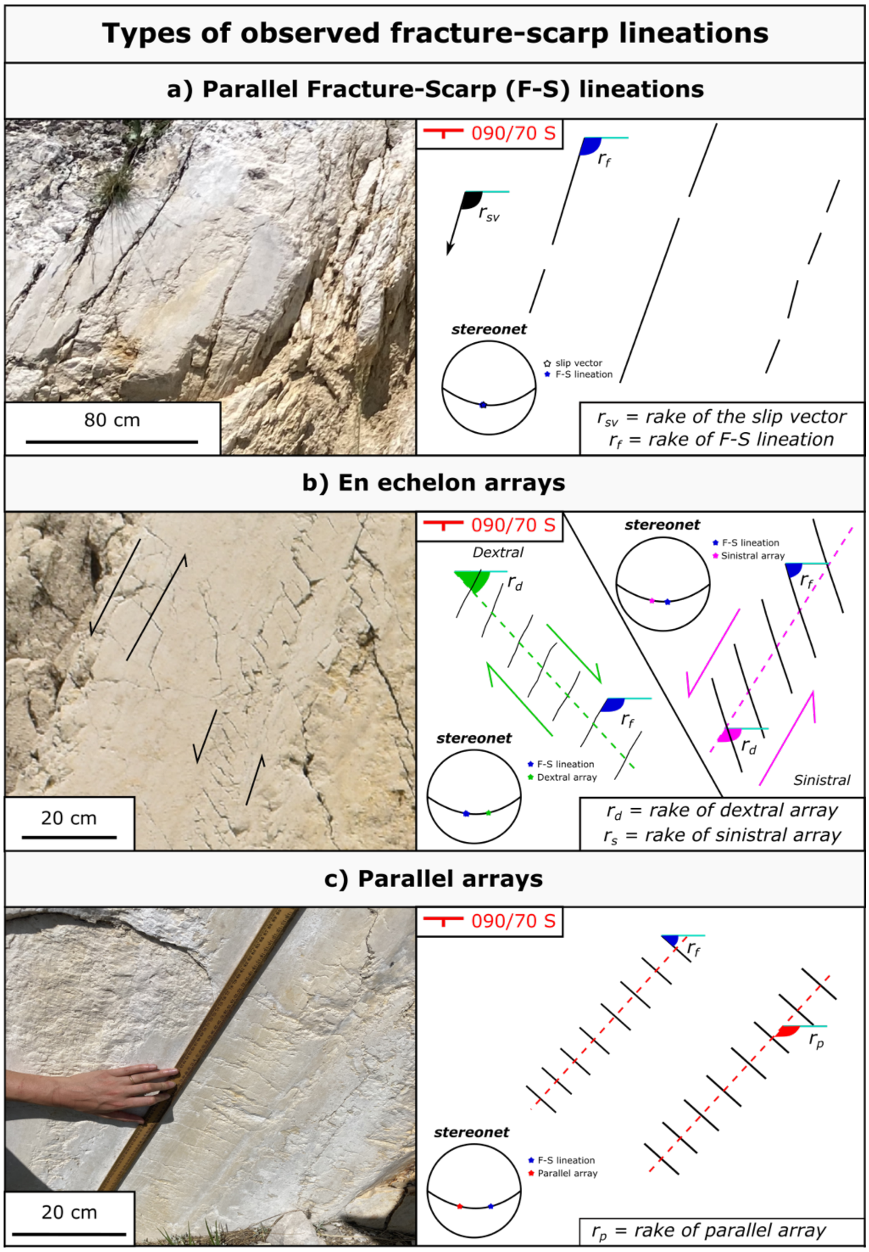

Figure 2: Types of fracture-scarp lineation: a) Parallel Fracture-Scarp (F-S) lineations that form along a single trend; b) En-echelon arrays consisting of smaller trace length F-S lineations that display sinistral or dextral shear sense; c) Parallel arrays that are similar to en-echelon arrays but show no shear sense.

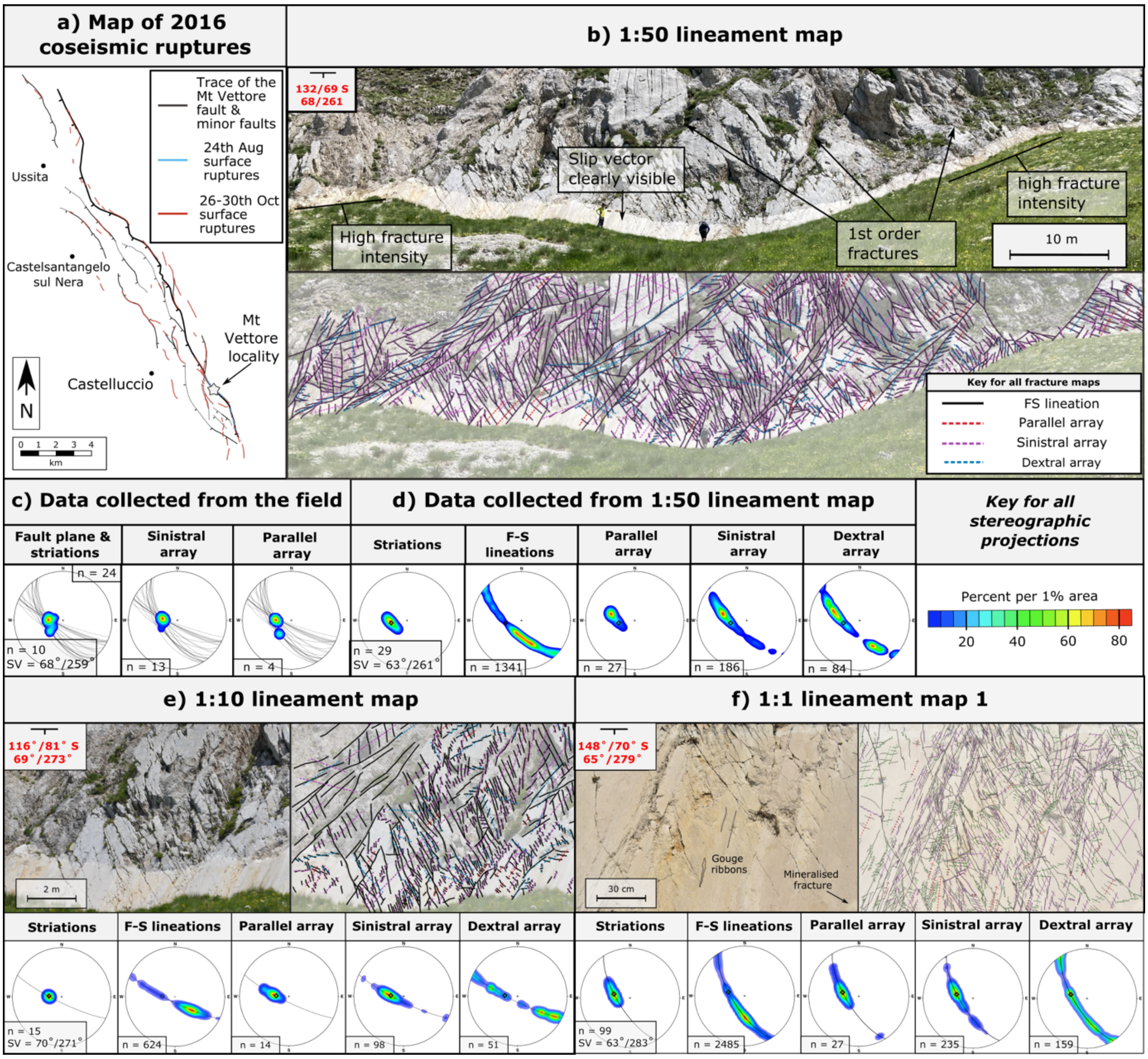

Figure 3: F-S lineation maps for the Mt Vettore location: a) trace of Mt Vettore showing the location of surface ruptures formed during the 2016 Central Italy earthquake sequence; b) uninterpreted photograph and 1:50 scale F-S lineation map; stereographic projections of data collected in the (c) field and (d) extracted from the 1:50 lineament map; uninterpreted photograph, lineament maps, and stereonets for the (e) 1:10 and (f) 1:1 scale F-S lineament map. SV = mean dip and plunge of the slip vector, n = number of data points.

956

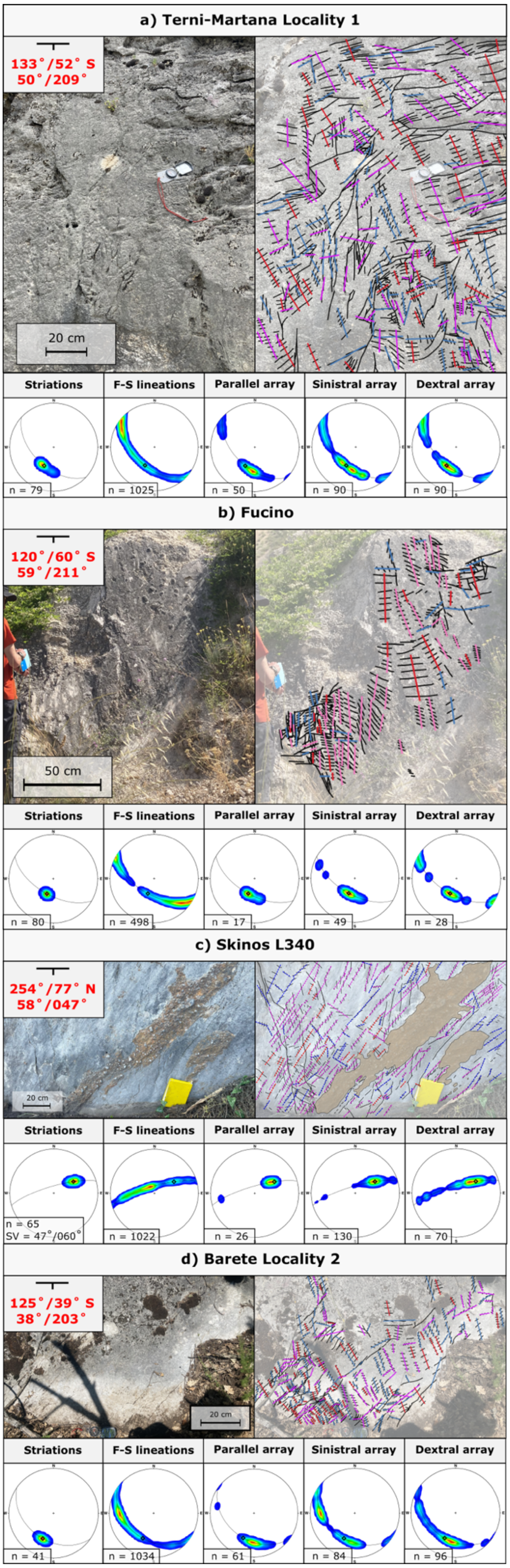

a) Terni-Martana Locality 1
133°/52° S
50°/209°
20 cm
Striations
F-S lineations
Parallel array
Sinistral array
Dextral array
n = 79
n = 1025
n = 50
n = 90
n = 90
b) Fucino
120°/60° S
59°/211°
50 cm
Striations
F-S lineations
Parallel array
Sinistral array
Dextral array
n = 80
n = 498
n = 17
n = 49
n = 28
c) Skinos L340
254°/77° N
58°/047°
Striations
F-S lineations
Parallel array
Sinistral array
Dextral array
n = 65
SV = 47°/060°
n = 1022
n = 26
n = 130
n = 70
d) Barete Locality 2
125°/39° S
38°/203°
Striations
F-S lineations
Parallel array
Sinistral array
Dextral array
n = 41
n = 1034
n = 61
n = 84
n = 96

Figure 4: Subsection of F-S lineation maps used in this study. Note, all maps are available in the supplementary information (S1, Figs S1-S6).

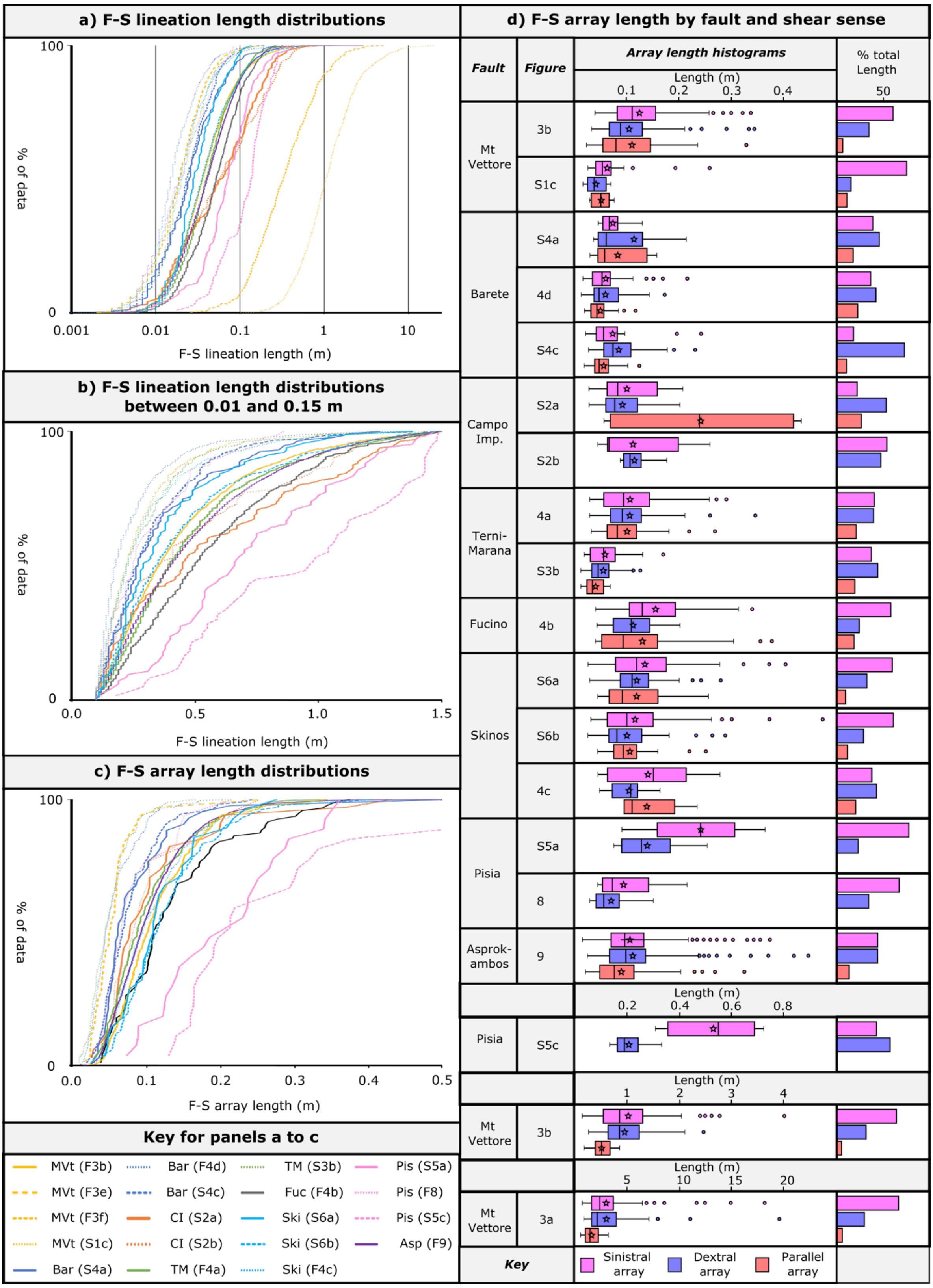

Figure 5: Trace length distributions of F-S lineations and arrays: a) F-S lineation length cumulative distributions; b) F-S lineation length cumulative distributions for features, with the x-axis clipped to between 0.01 and 0.15 m to show the distribution of small trace length features; c) F-S array length cumulative distributions; d) box and whisker plots of array length, and proportion of total length, split by the observed shear sense.

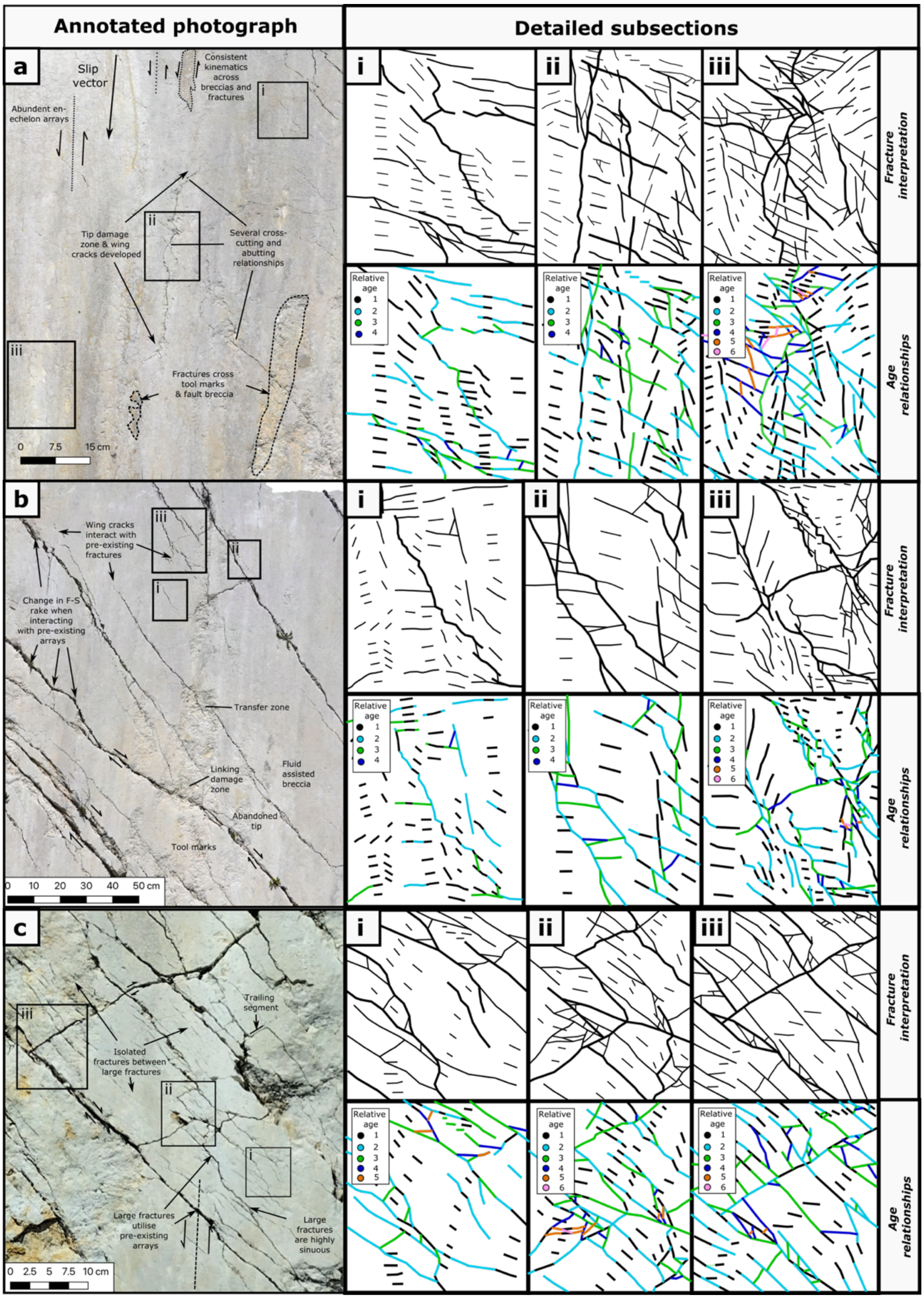

Figure 6: Relative age relationships observed across the white ribbon at Mt Vettore. Panels a-c show progressively more connected fracture networks and for each map, as evidenced by the increasing fracture intensity, connectivity, and abundance of linkage features (e.g., jogs, tip damage zones, sinuous fracrtures). In i-iii, we unpick age relationships for three

subsections using abutting and cross-cutting relationships. Note how during age relationship 1 (black lines) all fracture networks start as isolated en-echelon arrays and as the age relationships increase, fractures progressively increase in length causing fractures to abut against each other and the connectivity of the network increases.

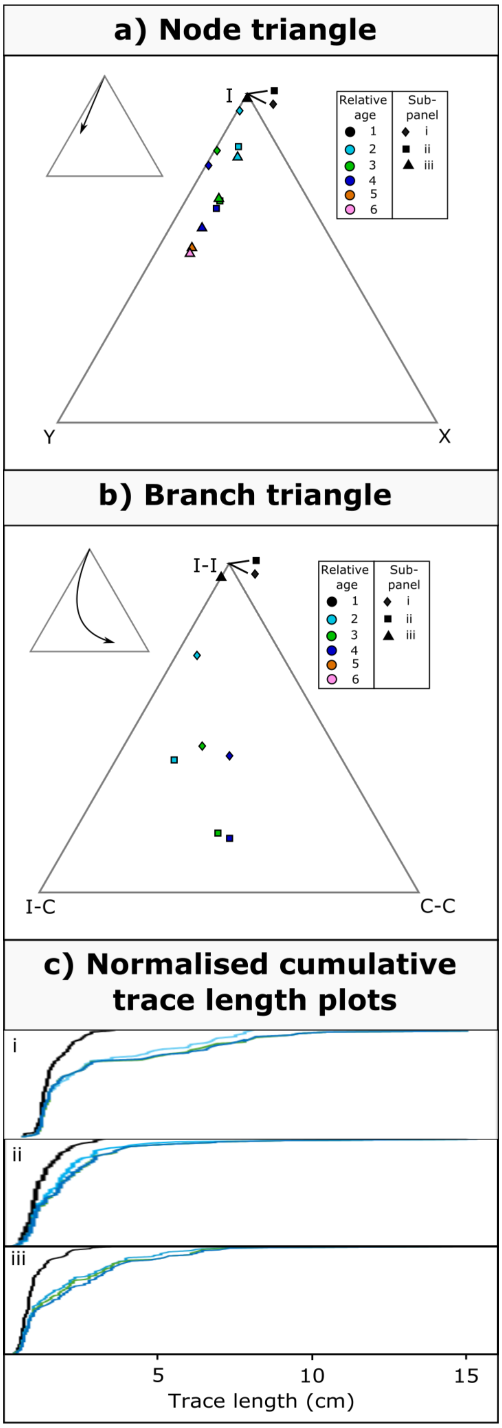

Figure 7: Topology and length evolution of the F-S lineation network extracted from the subpanels of the Mt Vettore fault scarp presented in Figure 6a. A) Node triangle showing the ratio of node types for the subsections of Figure 6a extracted at each relative age relationship; b) branch triangle showing the ratio of branch classification for the subsections of Figure 6a extracted at each relative age relationship; c) Normalised cumulative length plots showing the evolution of F-S length at each relative age relationship. Note how the connectivity and upper portion of the trace-length distribution increases as the fracture network develops.

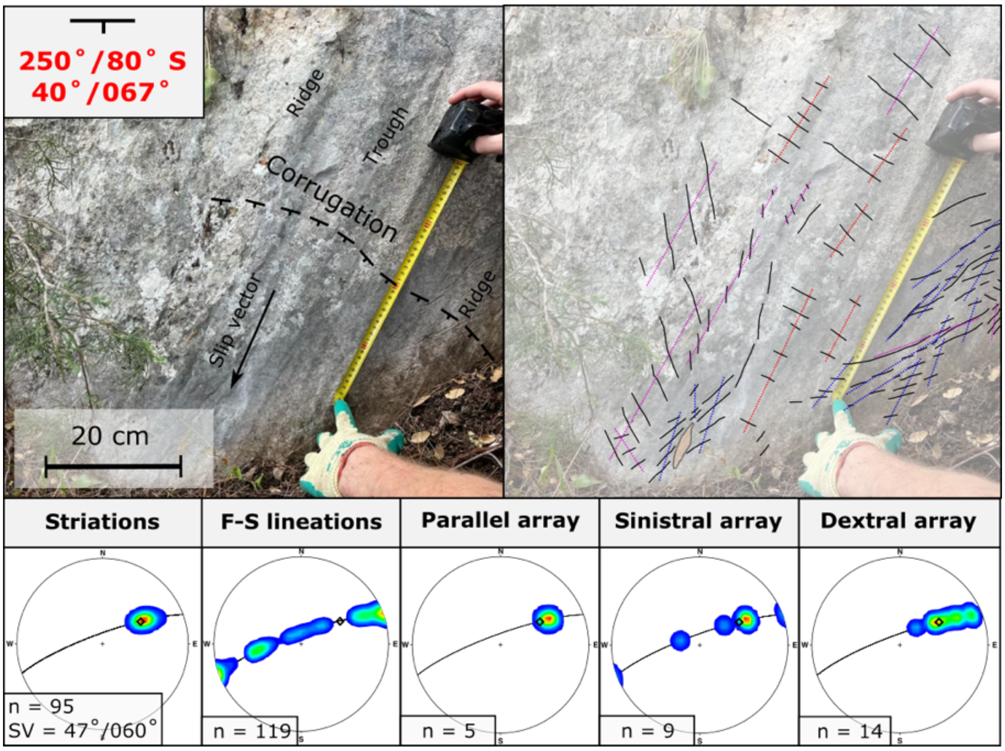

Figure 8: F-S lineations and arrays around a corrugation. Note how the orientation and kinematics of F-S lineation arrays differ either side of the corrugation.

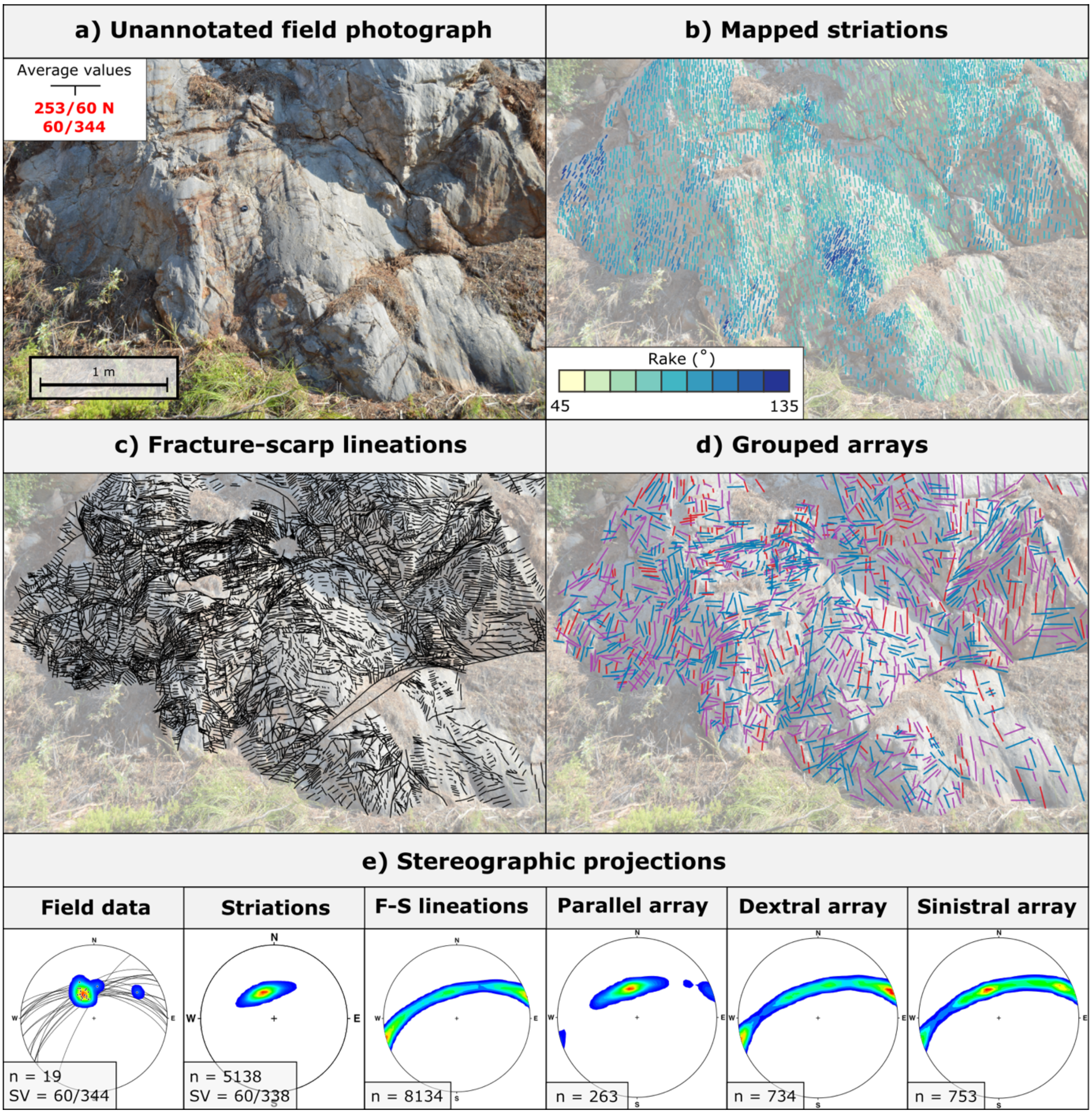

Figure 9: Distribution of (b) striations, (c) F-S lineations and (d) arrays across the Asprokambos fault locality; e) stereographic projections of field and photo derived data. Note how convergent and divergent slip vectors are recorded, and that in areas where shallower slip-vectors are observed, that the rake and shear sense of F-S arrays also differ.

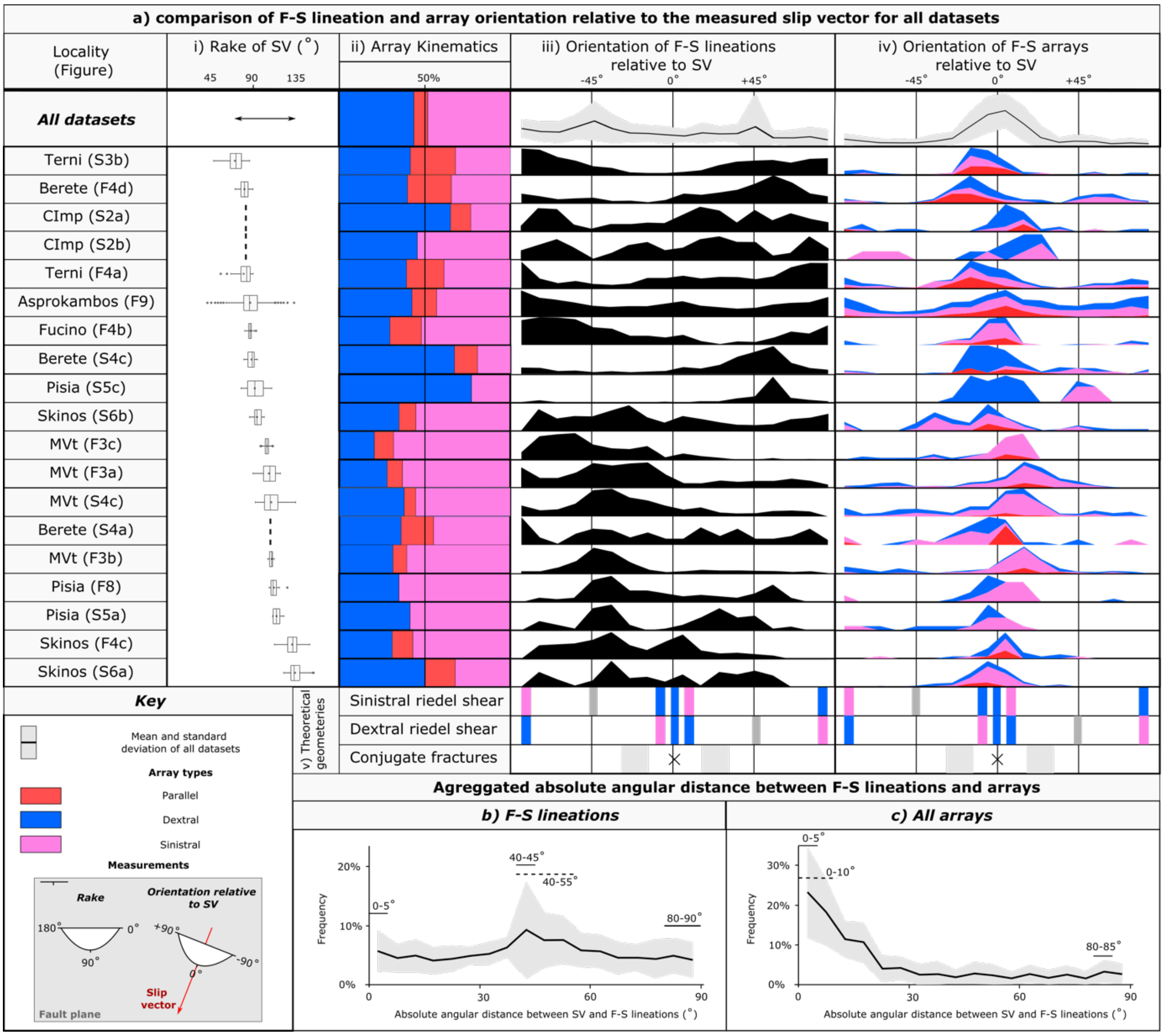

Figure 10: The orientation of F-S lineations and arrays relative to the slip vector: a) comparison of F-S lineation and array orientations with the measured slip vector, showing i) box and whisker plots of slip vector rake distributions, ii) the relative abundance of different shear sense arrays, normalised 10̊bin histograms of iii) F-S lineations and iv) arrays, where the y-axis is the maximum value for each F-S lineation map, and v) the expected orientations of features according to a radial shear geometry; normalised aggregated absolute angular distance between F-S lineations (b) and arrays (c) to the slip vector for all studied faults (see measurements in the key for how measurements are taken. Note the relationship between

slip vector rake and proportion of dextral to sinistral arrays, and the peaks observed in (b) and (c).

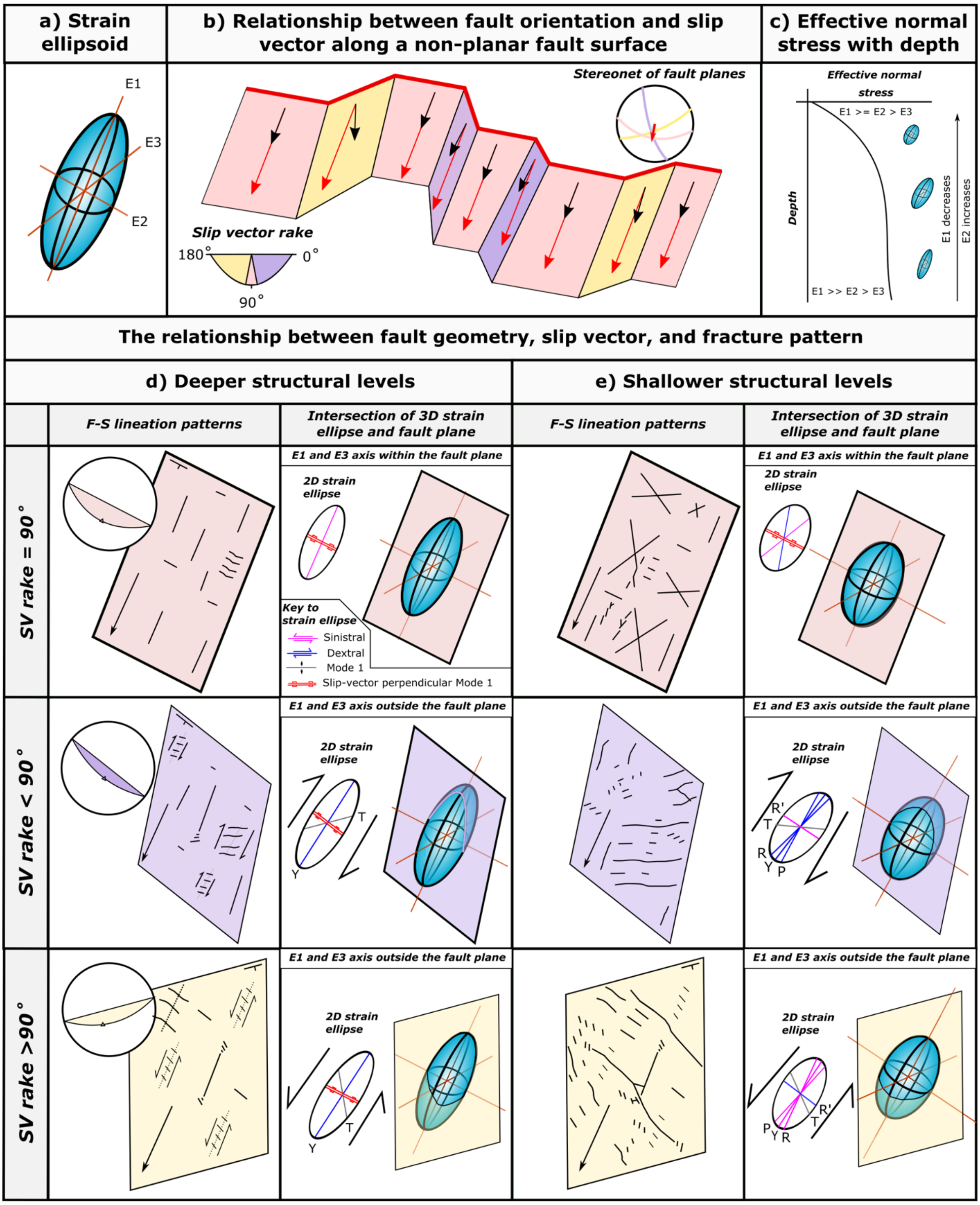

Figure 11: Conceptual model for the formation of F-S lineations and arrays: a) 3D strain ellipsoid, showing the three principle axes E1, E2 and E3; b) a schematic relationship

between fault plane geometry and slip vector around prominent fault bends whereby slip vector remains constant; c) the suggested effect of footwall uplift on the effective normal stress acting on the fault plane; the relationship between fault plane geometry, slip vector, the schematic expected fracture patterns, and the intersection of between the fault plane and 3D strain ellipsoid for the schematic fault orientations at (d) deeper and (e) shallower depths.

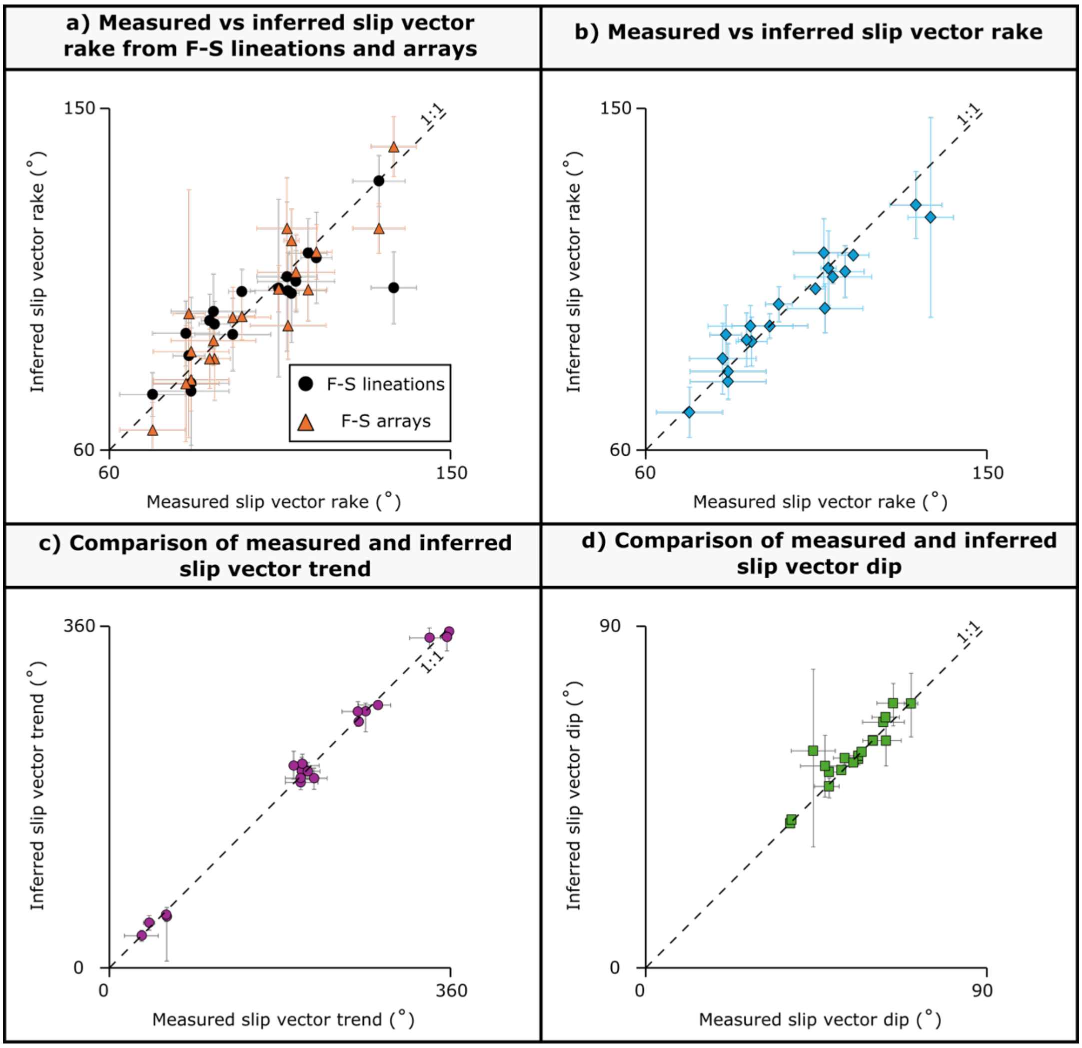

Figure 12: Comparing the measured slip vector from striations to slip vector inferred from F-S lineations for all F-S lineation maps: Reliability of assigning generic trends to individual faults when inferring slip vector: a) comparison of slip vector inferred using F-S lineations

(circles) and F-S arrays (triangles) with the slip vector measured from striations; b) comparison of averaged inferred slip vector using both F-S lineations and arrays with the slip vector measured from striations; c) comparison of the inferred slip-vector trend with that measured from striations; d) comparison of the inferred slip-vector dip with that measured from striations. For all plots, the error bars represent one standard deviation either side of the mean. Note how the average of F-S lineation and F-S array inferred rake (b) is closer to the measured rake than when they are considered separately.

Tables

Fault	Fig	Measured SV			Inferred SV			Difference between inferred and measured SV		
		Rake (°)	Dip (°)	Trend(°)	Rake (°)	Dip (°)	Trend(°)	Rake (°)	Dip (°)	Trend(°)
Barete	7a	107	52	216	97	55	200	9.7	3	15.7
	7b	80.9	38	203	90	39	216	9.5	1	12.1
	7c	87.7	38	207	89	38	208	0.9	0	1.1
Campo Imperatore	5a	81.5	56	202	78	55	196	3.4	1	5.9
	5b	81.5	56	202	81	56	200	0.8	0	1.4
Fucino	8	86.4	60	203	89	60	208	2.7	0	5.4
Mt Vettore	4c	104.6	52	263	103	52	260	2.0	1	3.1
	4a	108	70	270	108	70	271	0.3	0	0.4
	4b	109.2	63	284	106	65	277	3.5	2	6.1
	3	106.8	63	262	112	60	271	5.3	3	8.5
Pisia	9a	114.6	63	358	111	66	355	3.2	3	3.4
	9b	112.4	65	356	107	70	349	5.3	5	7.0
	9c	92.5	57	34	93	57	34	0.2	0	0.3
Skinos	10a	135	44	60	121	57	54	13.6	13	6.0
	10c	131.1	47	60	125	53	56	6.4	6	3.5
	10b	94.9	55	42	98	54	48	3.6	1	6.1
Asprokambos	12	87.4	60	338	93	60	348	5.3	0	10.6
Terni-Martana	6a	80.1	48	194	84	52	214	4.0	3	19.3
	6b	71.3	48	209	70	48	207	1.3	1	1.8

Table 1: Calculated slip vector from F-S lineations, see Supplementary 6 for calculation using F-S lineations and F-S arrays separately, and for the spreadsheet to calculate slip vector from rake clusters.

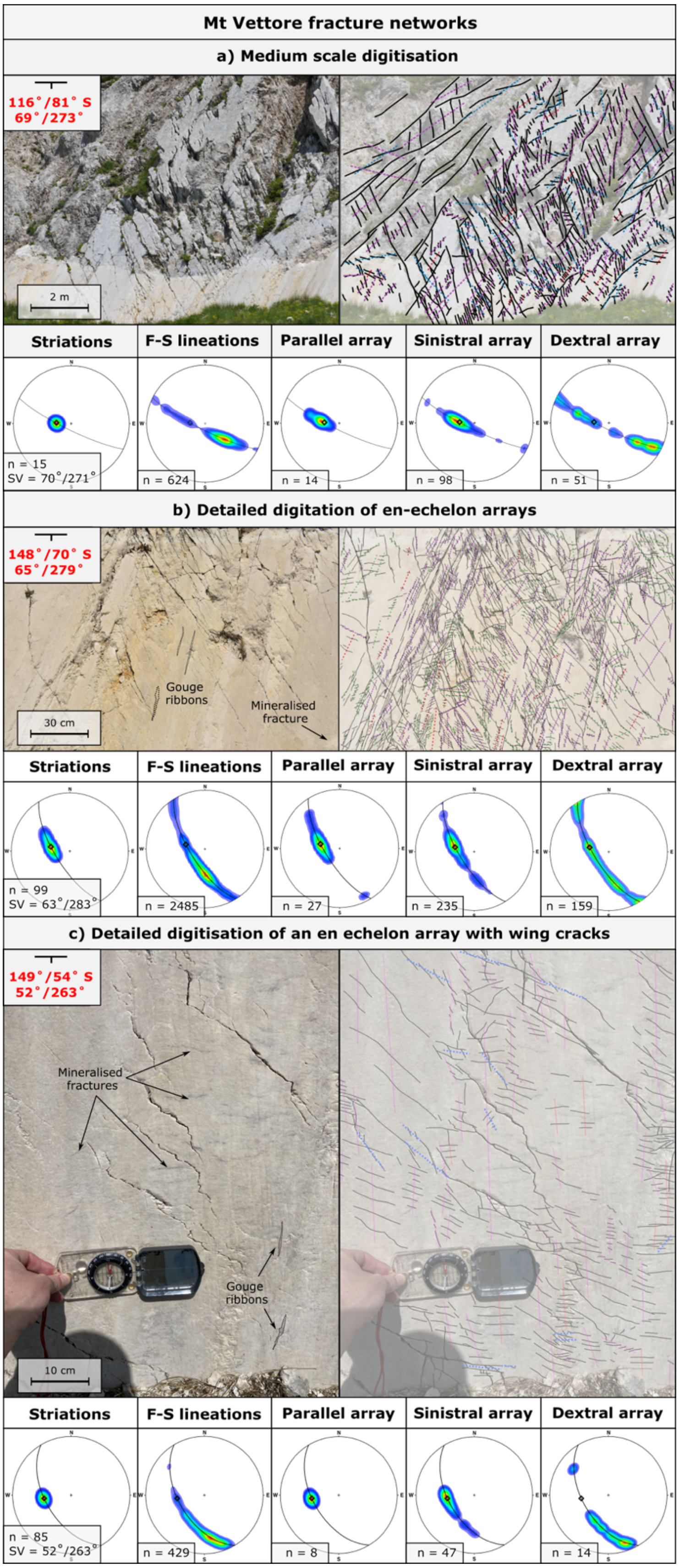

Figure S1: 1:10 and 1:1 F-S lineation and array maps across the Mt Vettore location.

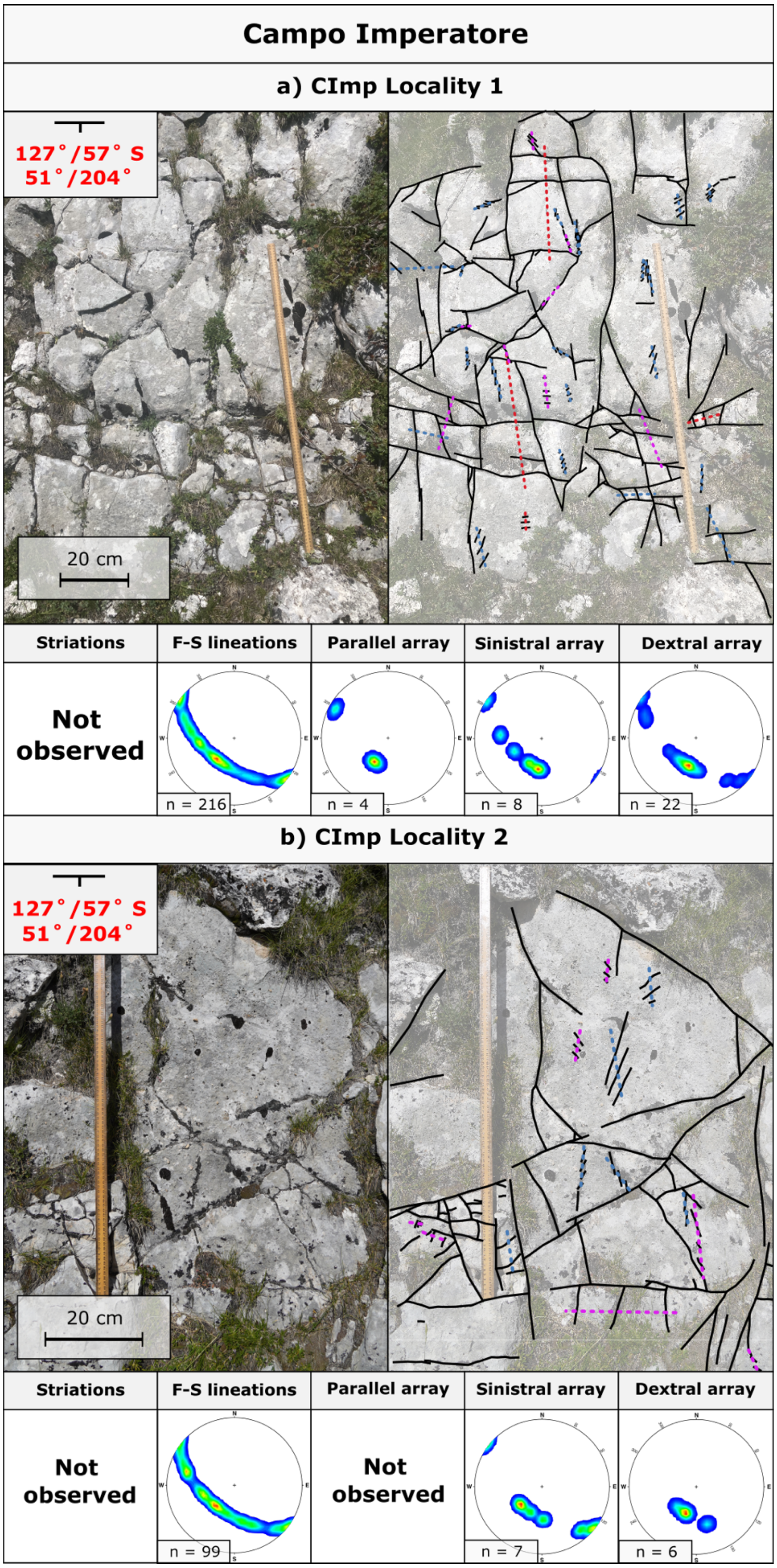

Figure S2: All F-S lineation and array maps across the Campo Imperatore location.

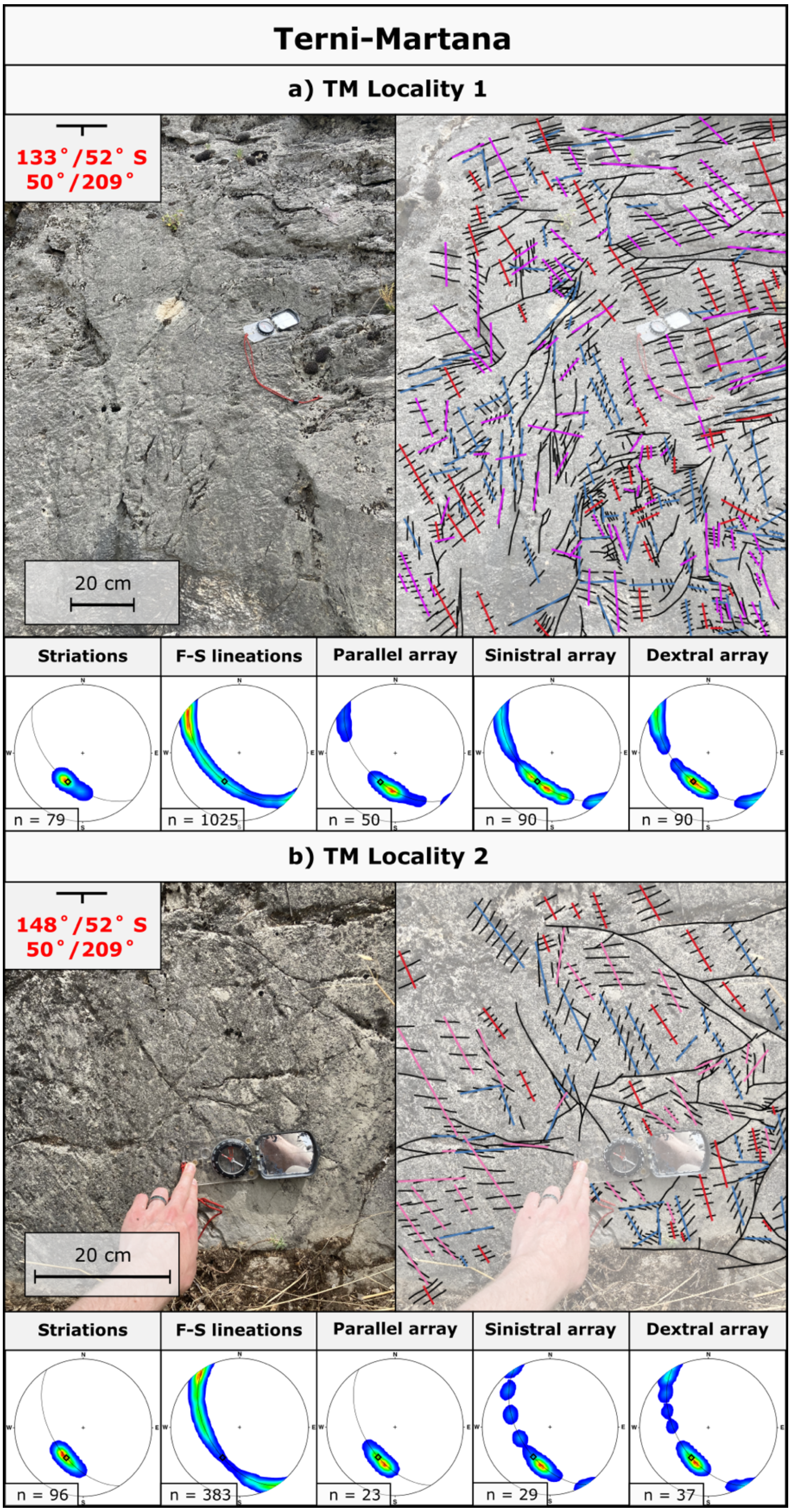

Figure S3: All F-S lineation and array maps across the Terni-Martana location.

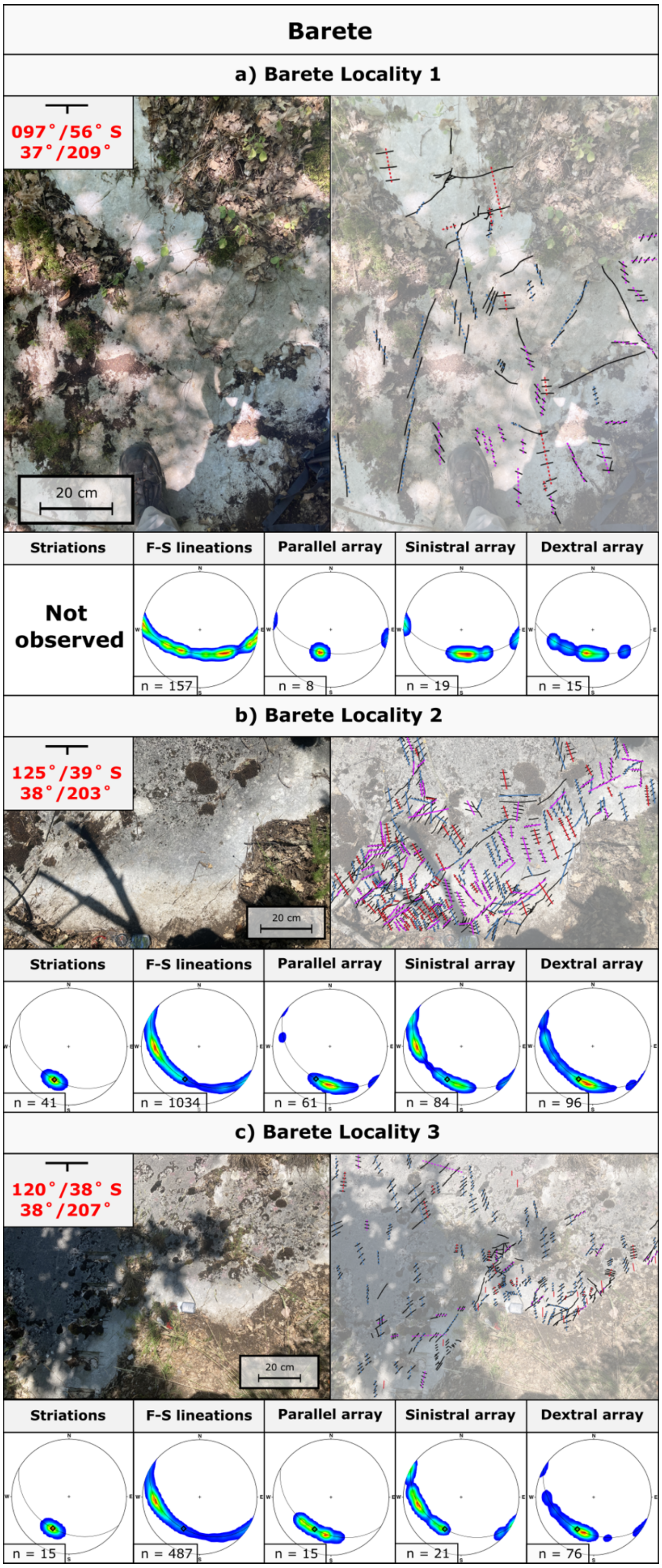

Figure S4: All F-S lineation and array maps across the Barete location.

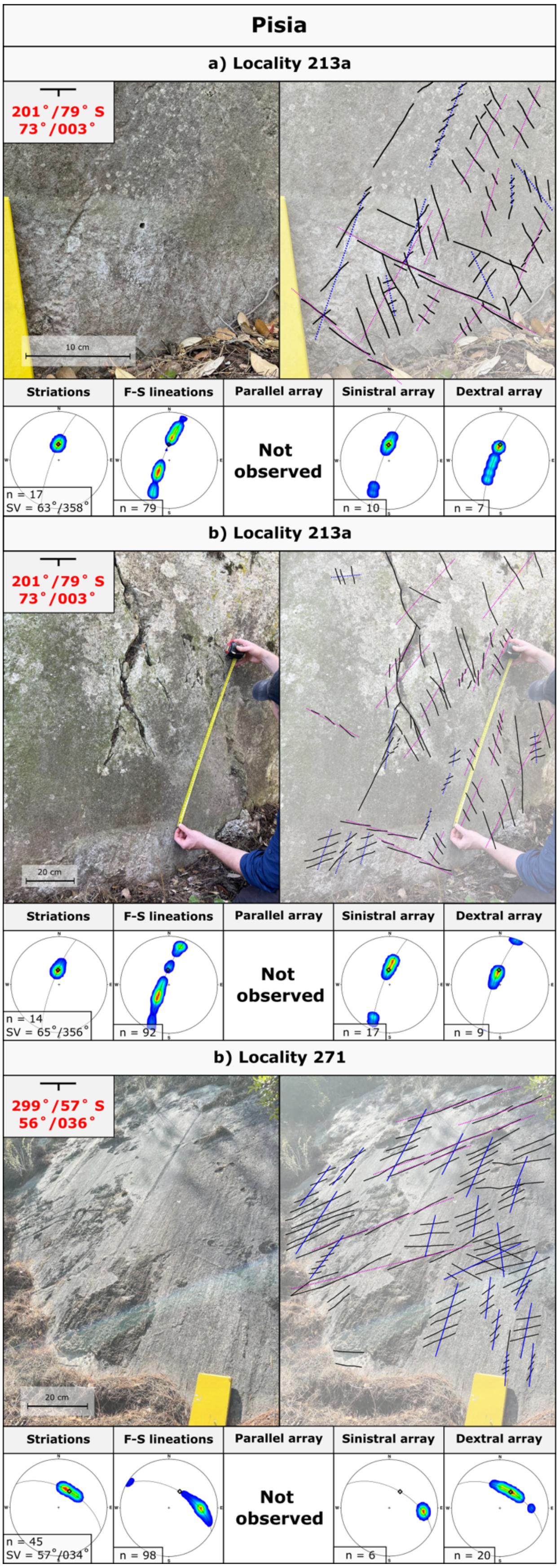

1035

1036 Figure S5: All F-S lineation and array maps across the Pisia location.

1037

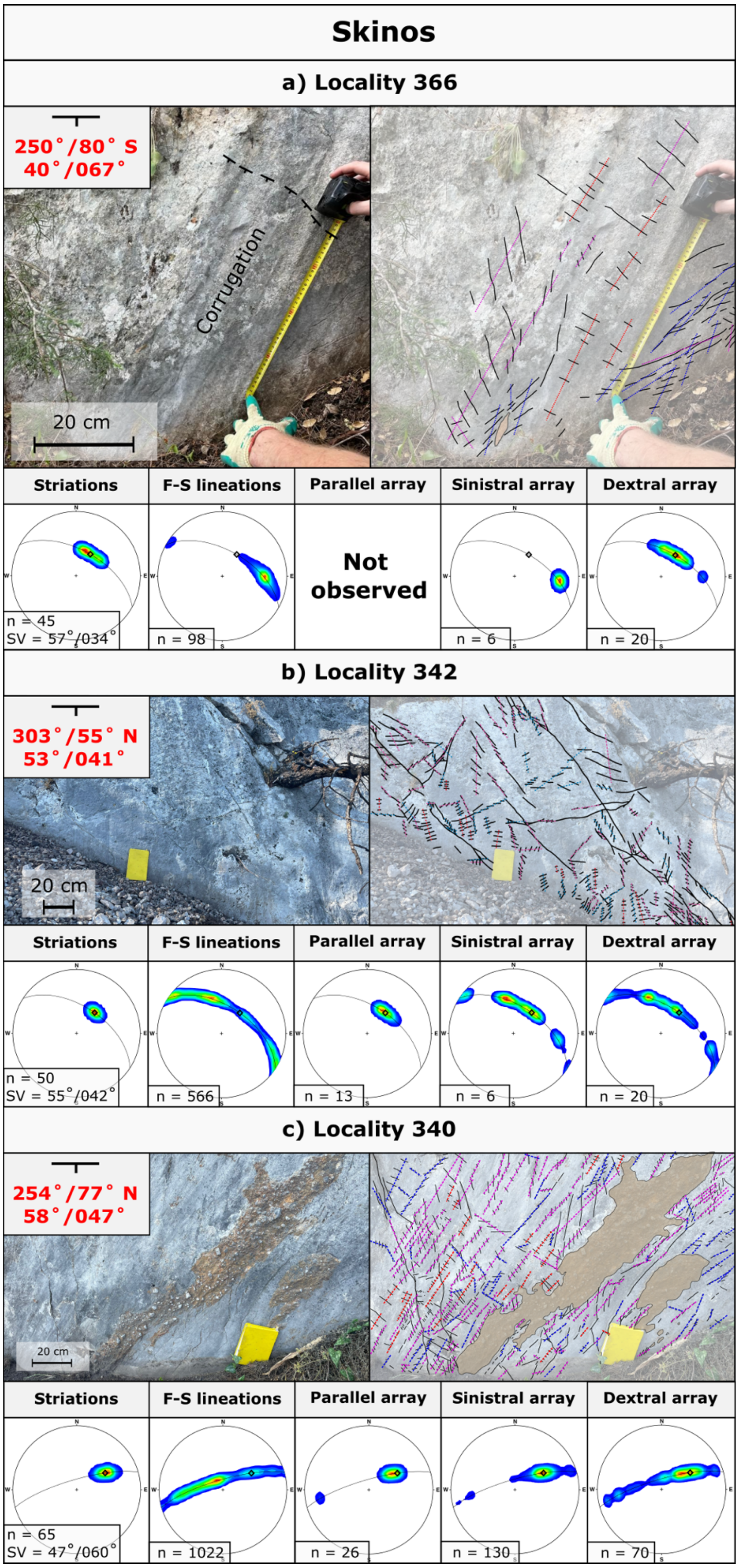

1038 Figure S6: All F-S lineation and array maps across the Skinos location.